Environment International 171 (2023) 107725

Contents lists available at ScienceDirect

Environment International

journal homepage: www.elsevier.com/locate/envint

Full length article

Secondary $PM_{2.5}$ dominates aerosol pollution in the Yangtze River Delta region: Environmental and health effects of the Clean air Plan

Nan Li [a,1], Haoran Zhang [a,1], Shuhan Zhu [a], Hong Liao [a,*], Jianlin Hu [a], Keqin Tang [a], Weihang Feng [b], Ruhan Zhang [c], Chong Shi [d], Hongmei Xu [e], Lei Chen [a], Jiandong Li [a]

[a] Jiangsu Key Laboratory of Atmospheric Environment Monitoring and Pollution Control, Jiangsu Collaborative Innovation Center of Atmospheric Environment and Equipment Technology, School of Environmental Science and Engineering, Nanjing University of Information Science & Technology, Nanjing, 210044, China
[b] Institute for Atmospheric and Earth System Research, Faculty of Science, University of Helsinki, Helsinki, 00014, Finland
[c] Department of Environmental Science and Engineering, Fudan University, Shanghai, 200438, China
[d] Aerospace Information Research Institute, Chinese Academy of Sciences, Beijing, 100094, China
[e] Department of Environmental Science and Engineering, Xi'an Jiaotong University, Xi'an, 710049, China

ARTICLE INFO

Handling Editor: Xavier Querol

Keywords:
$PM_{2.5}$ pollution
Premature mortality
WRF-Chem
YRD
Emission control

ABSTRACT

The Clean Air Plan has been active in China since 2013 to mitigate severe $PM_{2.5}$ pollution. In this study, we applied the air quality model WRF-Chem to simulate $PM_{2.5}$ in the Yangtze River Delta (YRD) region of China in 2017, with the aim of assessing the air quality improvement and its associated health burden in the final year of the Clean Air Plan. To better describe the fate of various $PM_{2.5}$ compositions, we updated the chemical mechanisms in the model beforehand, including heterogeneous sulfate reactions, aqueous secondary organic aerosol (SOA) uptake, and volatility basis set (VBS) based SOA production. Both the observation and simulation results agreed that the stringent clear air action effectively reduced the $PM_{2.5}$ pollution levels by ~ 30 %. The primary $PM_{2.5}$ ($-6 \sim -16$ % yr^{-1}) showed a more significant decreasing trend than the secondary $PM_{2.5}$ ($-2 \sim -8$ % yr^{-1}), which was mainly caused by the directivity of the clear air actions and the worsening ozone pollution in the recent years. The inconsistent decreasing trends of $PM_{2.5}$ components subsequently led to an increasing proportion of secondary $PM_{2.5}$. Nitrate particles, higher in the central and western YRD region, have replaced sulfate and have become the largest component of secondary inorganic aerosols year-round, except in summer, when strong ammonium nitrate evaporation occurs. In addition, SOA remains an important component (21 ~ 22 %) especially in summer, most of which is produced from the oxidation and ageing of semi/intermediate volatile organic compounds (S/IVOC). Furthermore, we quantified the associated health impacts and found that the Clean Air Plan has largely reduced premature mortality due to $PM_{2.5}$ exposure in the YRD region from 399.1 thousand to 295.7 thousand. Our study highlights the benefits of the Clean Air Plan and suggests that subsequent $PM_{2.5}$ improvement should be geared more towards controlling secondary pollutants.

1. Introduction

Particulate matter with an aerodynamic diameter of less than 2.5 μm ($PM_{2.5}$) is a major air pollutant that severely threatens public health (Guan et al., 2016). $PM_{2.5}$ comes from both primary emissions of anthropogenic or natural particles and secondary oxidation of reactive gases (Seinfeld and Pandis, 2006). Primary $PM_{2.5}$ includes primary organic aerosol (POA), elemental carbon (EC) and dust, mainly from combustion processes and flying dust (Zhang et al., 2021a). Secondary $PM_{2.5}$ is composed of secondary organic aerosol (SOA) and secondary inorganic aerosol, including sulfate (SO_4^{2-}), nitrate (NO_3^-) and ammonium (NH_4^+), i.e., SNA (Sulfate-Nitrate-Ammonium).

To mitigate the worsening $PM_{2.5}$ pollution, the China State Council implemented the Air Pollution Prevention and Control Action Plan, i.e., the Clean Air Plan, in 2013. This long-term policy aims at a 10 % reduction in the nationwide $PM_{2.5}$ concentration by the end of 2017. The Clean Air Plan conducts emission controls by eliminating backwards industries, implementing stricter vehicle emission standards and desulfurizing flue gas (Tang et al., 2019; Wu et al., 2017). Numerous studies have been carried out on interannual and regional variations in $PM_{2.5}$

* Corresponding author.
E-mail address: Hongliao@nuist.edu.cn (H. Liao).
[1] These authors contributed equally.

https://doi.org/10.1016/j.envint.2022.107725
Received 26 September 2022; Received in revised form 30 November 2022; Accepted 29 December 2022
Available online 30 December 2022

pollution since 2013 (An et al., 2019; Elser et al., 2016; Wang et al., 2016). Surface $PM_{2.5}$ measurements showed that the annual mean $PM_{2.5}$ concentration decreased by 30–50 % over the 2013–2018 period because of the Clean Air Plan (e.g. Zhai et al., 2019; Zhang et al., 2019). Moreover, aerosol composition studies revealed that the rapid decline in $PM_{2.5}$ by 9.1 % yr^{-1} was largely beneficial due to the decrease in SO_4^{2-} at a rate of –10.6 % yr^{-1} from 2013 to 2018 (Ding A. et al., 2019) mainly attributed to the unprecedented decrease in its precursor SO_2 (Chu et al., 2020), as well as the stringent control in primary composition (Li et al., 2022). Meanwhile, NO_3^- appeared a slight decreasing (even rising) trend during the same period, which can be mostly explained by higher conversion of gaseous nitric acid to particulate nitrate that slow down the deposition of total inorganic nitrate (Zhai et al., 2021).

Simultaneously, the $PM_{2.5}$-related environmental health burden, such as premature mortality, is also widely considered (Chen et al., 2020; Gao et al., 2018; Hu et al., 2017; Lin et al., 2021; Maji et al., 2018; Shen et al., 2020). All diseases associated with $PM_{2.5}$ exposure that led to premature death can be generally categorized into ischaemic heart disease (IHD), stroke, lung cancer (LC), chronic obstructive pulmonary disease (COPD), noncommunicable disease (NCD) and lower respiratory infections (LRI). Maji et al. (2018) reported annual premature mortality of up to 0.964 million based on ground-based observations in 338 cities in China. Moreover, Hu et al. (2017) applied the CMAQ model to estimate that 1.3 million premature deaths in China were attributable to $PM_{2.5}$ exposure in 2013. Some current studies explored the potential health impacts of the Clean Air Plan. Zhang et al. (2019) quantified the health benefits from specific clean air actions using a detailed emission inventory and further suggested the national avoided deaths to be 400 thousand in 2017. Dang et al. (2019) predicted 247–292 thousand fewer deaths in eastern China caused by the changes of both $PM_{2.5}$ and O_3 during 2012–2017. However, comprehensive studies focusing on trends, drivers and health benefits associated with the long-term control measures are still lacking.

In this study, we quantify the benefits of the emission reductions due to the Clean Air Plan in reducing both $PM_{2.5}$ concentration and the associated premature mortality in the Yangtze River Delta (YRD) region. We employed the air quality model WRF-Chem to simulate the $PM_{2.5}$ concentration and its chemical compositions and further compared the model results with multiple observations (Section 3). Subsequently, we investigated the spatiotemporal characteristics of various aerosol species as well as the premature mortality of $PM_{2.5}$ (Section 4). In addition, we quantified the long-term mitigative effect on $PM_{2.5}$ concentrations and the associated health burdens owing to the Clean Air Plan by setting a sensitivity experiment in Section 5. This study differs from previous works as follows: (1) we largely focus on the variations in $PM_{2.5}$ chemical positions during the execution of the Clean Air Plan, with the help of modified model simulations and multiple observations; and (2) we conducted sensitivity simulations to quantify both the environmental and health benefits of the long-term control measures in the YRD region.

2. Methods and materials

2.1. Air quality model

2.1.1. WRF-Chem

WRF-Chem is an open-source mesoscale air quality model developed by the National Center for Atmospheric Research (NCAR) of the United States. This model can simulate atmospheric chemical reactions with fully coupled meteorology-chemistry processes (Fast et al., 2006; Grell et al., 2005) and is widely used by the scientific community for air quality modelling studies (Gochis et al., 2017; Li et al., 2018; Shrivastava et al., 2019; Zhang et al., 2021b). WRF-Chem inherits the dynamics and physical framework from its parent model WRF. The model adopts diverse physical parameterization schemes for describing subgrid processes, including radiative feedback, horizontal advection, vertical diffusion and dry and wet depositions. Table S1 lists the specific physical parameterizations used in this study (Chen and Dudhia, 2001; Grell and Dévényi, 2002; Iacono et al., 2008; Jimenez et al., 2012; Morrison et al., 2009; Nakanishi and Niino, 2006). To conduct the meteorological simulation, we derived the global FNL reanalysis datasets as initial and boundary conditions from the U.S. National Centers for Environmental Prediction (NCEP, *https://rda.ucar.edu/datasets/ds083.2/*, last accessed on 19 December 2021). The temporal and spatial resolutions of the FNL data are 6 h and 1° × 1°, respectively. For chemistry, we utilized the Statewide Air Pollution Research Center mechanism (SAPRC99) as the gas phase chemical parameterization scheme (Carter, 2000). SAPRC99 comprises 74 kinds of gases and 211 kinds of related chemical reactions. The fast-J parameterization scheme was selected for modelling photolysis processes (Wild et al., 2000). We chose the Model for Simulating Aerosol Interactions and Chemistry (MOSAIC) as the aerosol parameterization scheme to predict the speciation, thermodynamic process and size distribution of aerosols (Zaveri et al., 2008). In general, MOSAIC divides the particle size of aerosols into eight intervals. To reduce computational costs and storage burdens, we merged every-two neighbouring intervals. The simplified particle diameter is then distributed within 4 bins, i.e., 0.039–0.156 μm, 0.156–0.625 μm, 0.625–2.500 μm and 2.500–10.000 μm. MOSAIC categorizes aerosol species into SO_4^{2-}, NO_3^-, NH_4^+, EC, OC, sea salt (Na^+ and Cl^-) and other inorganic aerosols. However, MOSAIC assumes that OC only comes from primary emissions. With the aim of predicting SOA, we implemented the VBS framework and aqueous reactions of dicarbonyl in the revised WRF-Chem model. In addition, we considered the heterogenous reaction of SO_4^{2-} to better represent the formation of secondary inorganic aerosols, which may be a crucial factor for explaining haze events in China (Cheng et al., 2016; Wang et al., 2016). The updated aerosol parameterizations are elucidated in Sections 2.1.2 and 2.1.3. Initial and boundary conditions of chemical species were given by the global Model for Ozone and Related Chemical Tracers (MOZART) developed by Emmons et al. (2010).

We configured two nested domains for this study (Fig. 1). The parent domain (d01) covers China, with a horizontal resolution of 36 km × 36 km. The child domain (d02), which has a horizontal resolution of 12 km × 12 km, is in eastern China, covering the entire YRD region. The number of grid cells in d01 and d02 is 146 × 116 (columns × rows) and 90 × 90, respectively. The YRD region is defined as Shanghai as well as most cities in the Jiangsu, Zhejiang and Anhui Provinces. The complete list of 26 cities in the YRD region can be found in Table S2. We set 28 vertical levels from the surface to a height of 50 hPa by means of the σ coordinate. The 7 bottommost layers are distributed below the typical boundary layer (~1 km). The base case of the WRF-Chem simulation is conducted in 2017, which is the final year of the Clean Air Plan. Simulations were conducted in January, April, July and October to represent the seasonal variations. The first 48 h of each simulated month were reserved as the spin-up period of the numerical model. More model settings used in this study are available in Table S1.

2.1.2. Updating the heterogeneous uptake pathway of SO_4^{2-} formation

The impact of the heterogeneous uptake of SO_4^{2-} was demonstrated to be nonnegligible during past haze events in China. Implementation of this reaction in an air quality model can close the gap to reproduce the concentration of SO_4^{2-} during haze events. Therefore, the heterogeneous uptake pathway of SO_4^{2-} has been included in offline regional air quality models, such as CMAQ (Zheng et al., 2015) and CAM_x (Huang et al., 2019). For the online model, Ma et al. (2020) added this reaction in WRF-Chem (v3.6.1) based on the chamber model (Wang et al., 2016). We followed this framework and implemented this parameterization into WRF-Chem (v3.9.1). The production rate for the heterogeneous uptake of SO_4^{2-} is determined by the following equation.

$$\frac{d\left[SO_4^{2-}\right]}{dt} = \frac{1}{4}\gamma\nu S_c[SO_2] \quad (1)$$

where $\frac{d[SO_4^{2-}]}{dt}$ denotes the production rate of SO_4^{2-} (unit: ppm·s^{-1}); γ

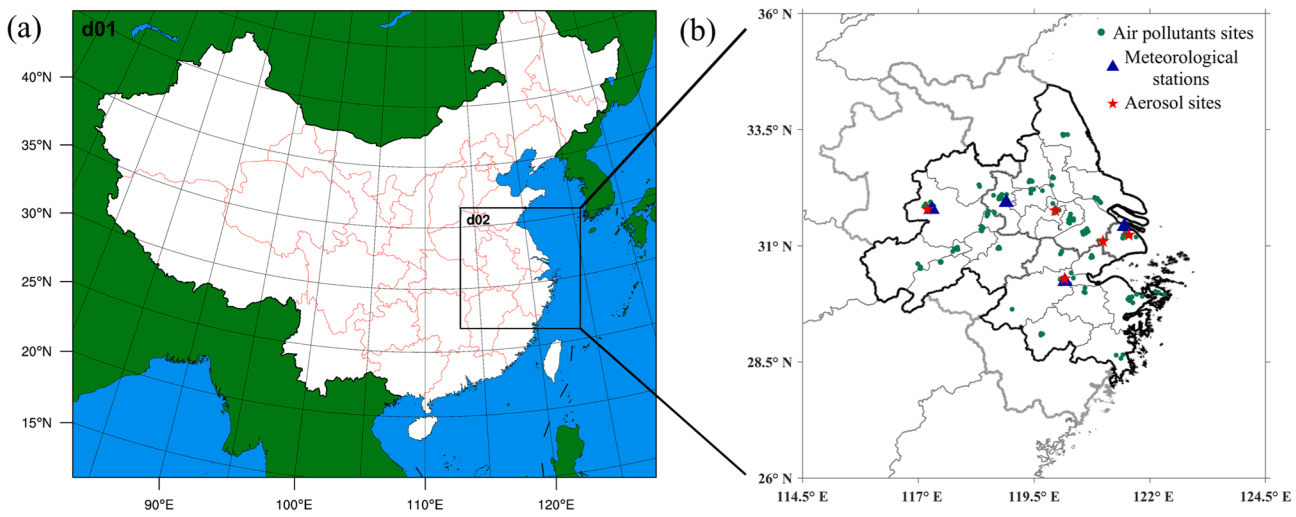

Fig. 1. WRF-Chem simulation domains and the observational sites across the YRD region in this study. (a) Spatial illustration of the simulated nested domains, with Lambert conformal as projection. D01 indicates the parent domain (most regions of China), with a central location of 104 °E, 33.5 °N. D02, which includes the YRD region, is the nested domain. (b) Geographical distributions of the sites for various observation, including air pollutants, meteorological parameters, and aerosol compositions, which are represented by dark green circles, blue triangles as well as red pentagrams respectively.

indicates the uptake coefficient for SO_2 on wet aerosol surfaces (unitless); v is the mean molecular velocity of SO_2 (unit: $m{\cdot}s^{-1}$); S_c represents the aerosol surface area density (unit: $m^2{\cdot}m^{-3}$); and $[SO_2]$ is the volume concentration (unit: ppm). The parameter γ is highly dependent on ambient relative humidity (RH), as shown in Eq. (2).

$$\gamma = \begin{cases} 1.6 \times 10^{-5} & RH < 41\% \\ 2.1 \times 10^{-5} & 41\% \leqslant RH \leqslant 56\% \\ 4.5 \times 10^{-5} & RH > 56\% \end{cases} \quad (2)$$

2.1.3. Updating the SOA simulation

Organics are simply treated as POA in the original MOSAIC model, lacking the representation for SOA. However, this kind of simplification is inappropriate because SOA is vital to $PM_{2.5}$ speciation. The traditional solution to estimate SOA concentrations is the two-product model (Odum et al., 1996), which tends to poorly underestimate SOA yields (Han et al., 2016). This bias could be solved by considering the SOA that evolves from semi/intermediate volatile organic compounds (S/IVOCs) (Li et al., 2011; Robinson et al., 2007; Tsimpidi et al., 2010). Thus, VBS is presented to describe the complete oxidation and ageing process of both VOCs and S/IVOCs (Qi et al., 2017) by using a logarithmic interval to indicate volatility with various effective saturation concentrations (C^*, at 298 K ambient temperature and 1013.25 hPa barometric pressure) from 10^{-2} to 10^6 $\mu g{\cdot}m^{-3}$. According to the VBS framework, C^* of the lumped VOC species exists within the range from 10^0 to 10^3 $\mu g{\cdot}m^{-3}$. The explicit VOCs comprise ALK4/ALK5, OLE1/OLE2 and ARO1/ARO2, which represent alkanes, alkenes and aromatics from anthropogenic activities or biomass burning. ISOP, TERP and SESQ are also included to denote isoprene, monoterpene and sesquiterpene from biogenic sources. The stoichiometric yields of SOA for these explicit VOC species under high or low NO_x concentrations are derived from Matsui et al. (2014). Different from VOC species, SVOCs are defined as implicit species with corresponding C^* values from 10^{-2} to 10^3 $\mu g{\cdot}m^{-3}$. For IVOCs, C^* varies from 10^4 to 10^6 $\mu g{\cdot}m^{-3}$. Reportedly, SVOC emissions are 3 times higher than POA emissions, and IVOC emissions are 1.5 times higher than SVOC emissions (Hodzic et al., 2010; Tsimpidi et al., 2010). Hence, a total of 7.5 times the POA emissions are estimated as S/IVOC emissions. Although VBS can capture the evolution of organic vapours as completely as possible, the computational costs are too large to efficiently run. Hence, we applied the condensed VBS scheme to save cost by following Shrivastava et al. (2011). The simplified VBS uses less running time and computation memory under the premise of predicting SOA formation well.

Another indispensable pathway for SOA production is the aqueous reactive uptake of dicarbonyl compounds, including glyoxal (GLY) and methylglyoxal (MGLY). It was revealed that SOA-produced via aqueous reactions (aq-SOA) accounted for 28–53 % of the total SOA in China according to previous model studies (Li et al., 2013; Xing et al., 2019). For this study, we also considered the irreversible uptake of dicarbonyl on aqueous phase surfaces in the YRD region. WRF-Chem only contains the aqueous reaction of GLY in the aerosol module, which is coupled with MOZART gas phase parameterization. Therefore, we revised MOSAIC to implement this reaction for both GLY and MGLY based on the SAPRC99 scheme. The related reactive uptake rate of dicarbonyl compounds follows Eq. (3).

$$\frac{d[\rho_{dicarbonyl}]}{dt} = \frac{1}{4}\gamma v S_c [\rho_{dicarbonyl}] \quad (3)$$

Parameter $\rho_{dicarbonyl}$ in Eq. (3) denotes the concentration of dicarbonyl in the gas phase (unit: ppm). Symbols v and S_c in Eq. (3) are the same as those in Eq. (1). The uptake coefficient γ of dicarbonyl compounds is an investigative value with large uncertainty (Li et al., 2013; Ling et al., 2020; Qiu et al., 2020). Here, we adopted $\gamma = 1.0 \times 10^{-3}$ to describe the uptake of dicarbonyl on the surface of wet particles (Knote et al., 2014). In addition, the Henry's law constants of GLY and MGLY were also updated in our revised model (Kampf et al., 2013; Sander, 2015).

2.1.4. Emissions and sensitivity experiment setups

Anthropogenic, biogenic and biomass burning emissions were collected as the emission inputs of the WRF-Chem model. In terms of anthropogenic emissions, the Multiresolution Emission Inventory for China (MEIC) developed by Tsinghua University (Li et al., 2017) was employed (*https://meicmodel.org/*, last accessed on 19 December 2021). The horizontal resolution of MEIC is 0.25° × 0.25°. Moreover, an emission inventory with a higher spatial resolution (4 km × 4 km) was used to reflect the local emission patterns over the YRD region (An et al., 2021; Zhou et al., 2017). All anthropogenic activities are categorized into industry, power, residential sources, agriculture and traffic transportation. Based on the statistics of MEIC, during the period from 2013 to 2017, it is revealed that SO_2, NO_x, CO, NH_3, EC, OC, $PM_{2.5}$ and PM_{coarse} emissions in the YRD region decreased by 65 %, 19 %, 25 %, 9 %, 26 %, 32 %, 33 % and 40 %, respectively (Table S3). However, VOCs emissions exhibit an increase of 3 %. The spatial distributions of these emissions are also illustrated in Fig. S1. The fine mode dust emissions are

inferred by deducting the emissions of primary sulfate, nitrate, EC and OC from the $PM_{2.5}$ emissions according to MEIC inventory. The simulation of dust concentrations in YRD regions were directly affected by the intensities of fine mode dust emissions. The Model of Emissions of Gases and Aerosols from Nature (MEGAN) was utilized for online calculation of biogenic emissions (Guenther et al., 2006). It is found that isoprene is the dominant biogenic VOCs species (40.3×10^4 ton in 2017) in the YRD region, which contributes to over 40 % of total biogenic emissions. Meanwhile, summertime produces more biogenic emissions that can occupy 74 % of annual total biogenic emissions. For biomass burning, the real-time Fire INventory from NCAR (FINN) was applied, which is based on remote sensing by the MODIS instrument onboard the satellite (Wiedinmyer et al., 2011). NO_x emission from lightning is not considered in this study since the emission from the high-altitude sources slightly affect the surface aerosol pollution in the YRD urban agglomeration (Dang et al., 2021).

To quantify the role that the reduction in anthropogenic emissions plays in alleviating aerosol pollution, we conducted a sensitivity experiment. We mark the base case and the sensitivity experiment as ANTH_17 and ANTH_13, respectively. To avoid the diverse meteorological effects in 2013 and 2017, ANTH_13 has the same initial and boundary conditions in the meteorological fields as ANTH_17 (Table S4). The fixed meteorological conditions can ensure that the relative changes in $PM_{2.5}$ concentrations and compositions are totally attributed to the long-term emission controls. Moreover, biogenic and biomass burning emissions are also fixed in ANTH_13. Only the anthropogenic emissions differ between ANTH_13 and ANTH_17, where ANTH_13 employs the emission level of 2013, which is the first year of the Clean Air Plan. The difference between the two simulations can uncover the impact of the long-term control measures of the Clean Air Plan. Notably, we did not use the YRD-specific emission inventory in ANTH_13 owing to the lack of data in 2013, and it is replaced by MEIC.

2.2. $PM_{2.5}$ health burden

2.2.1. Calculation of relative risks

One of the state-of-the-art methods used for estimating premature mortality caused by $PM_{2.5}$ exposure is the integrated exposure–response (IER) model developed by Burnett et al. (2014). The IER model coupled with the regional air quality model is widely applied for assessing the health burdens of air pollution (Gao et al., 2018; Hu et al., 2017). The first step to drive the IER model is calculating the relative risk (*RR*). The calculation of *RR* follows Eq. (4):

$$RR(C) = \begin{cases} 1 + \alpha\left(1 - e^{[-\beta(C-C_0)^{\delta}]}\right) & C \geqslant C_0 \\ 1 & C < C_0 \end{cases} \quad (4)$$

where α, β and δ indicate the fitted parameters based on the data under $PM_{2.5}$ exposure for various diseases. C denotes the annual mean $PM_{2.5}$ concentration ($\mu g \cdot m^{-3}$). In this model-based study, C refers to the average of the simulated $PM_{2.5}$ in each grid cell. C_0 is the threshold of $PM_{2.5}$ concentration that can induce health burdens ($\mu g \cdot m^{-3}$). If C is less than C_0, no risk of $PM_{2.5}$ exposure is considered, i.e., $RR = 1$. Otherwise, *RR* can be inferred via the exponential function. The fitted parameters of premature mortality for IHD, stroke, LC and COPD are provided by Lin et al. (2021) and summarized in Table S5.

In addition, Burnett et al. (2018) developed the Global Exposure Mortality Model (GEMM) which relied on 41 cohort studies of outdoor $PM_{2.5}$ from 16 countries, including a study of Chinese men with long-term outdoor $PM_{2.5}$ exposures up to 84 $\mu g \cdot m^3$. Compared to IER model, GEMM relaxed several strong assumptions and is assumed to provide robust estimates for highly polluted environments such as China. $GEMM_{NCD+LRI}$ model considers broader causes of deaths, including the sum of NCD and LRI in addition to aforementioned causes of death.

RR in $GEMM_{NCD+LRI}$ is calculated by Eq. (5):

$$RR(C) = \exp\left(\frac{\theta \log\left(1 + \frac{C - C_0}{\partial}\right)}{1 + \exp\left(-\frac{(C - C_0) - \mu}{\upsilon}\right)}\right) \quad (5)$$

Where ∂, μ, ν and θ are fitted parameters which shaped the relationship between long-term exposure to outdoor $PM_{2.5}$ and mortality (Table S6). C_0 in GEMM model is set as 2.4 $\mu g \cdot m^{-3}$.

2.2.2. Calculation of premature mortality

After accessing RR, premature mortality (Mort) for both IER and GEMM can be calculated using Eq. (6).

$$Mort = y_0 \times P \times \frac{RR - 1}{RR} \quad (6)$$

In Eq. (6), y_0 is the baseline mortality of the specific disease among the population in China. y_0 stands for various diseases and ages and can be obtained from the Global Burden of Disease (GBD) database (https://vizhub.healthdata.org/gbd-compare/, last accessed on 19 December 2021). P represents the gridded population data with a horizontal resolution of $0.0083^\circ \times 0.0083^\circ$, which was derived from the Gridded Population of the World database developed by the U.S. NASA (GPW version 4, https://sedac.ciesin.columbia.edu/data/collection/gpw-v4/whatsnewrev11, last accessed on 19 December 2021). The original GPW data were reallocated to match the grids of the WRF-Chem model.

In this study, we compare the results of IER and GEMM models (Table S7) and find that the $PM_{2.5}$ exposure impact estimated by IER is ~ 50 % of that by GEMM, and we choose $GEMM_{NCD+LRI}$ model to predict the premature mortality in the YRD region, as it includes broader causes of deaths.

2.3. Observations

2.3.1. Meteorological parameters and air pollutants

We obtained ground observations, including temperature, RH, wind speed and wind direction (http://www.meteomanz.com/, last accessed on 19 December 2021) to validate the simulation of meteorological parameters. Data from this repository were updated every 3 h. In addition, surface observations of the air pollutants were also collected to evaluate the simulation of gases (i.e., O_3, NO_2, SO_2 and CO) and aerosols ($PM_{2.5}$ and PM_{10}). Hourly data records of air pollutants are available at the public website of the Ministry of Ecology and Environment, China (https://106.37.208.233:20035/, last accessed on 19 December 2021). In general, we selected four meteorological stations and 136 air quality sites to assess the model performance of routine meteorological parameters and air pollutants over the YRD region. Complete information on the observational sites can be found in Table S2. Simultaneously, Fig. 1 also illustrates the geographical locations of these sites.

2.3.2. Aerosol composition measurements

One-year in situ $PM_{2.5}$ composition observations at five sites over the YRD region were obtained by Shanghai Academy of Environment Sciences in 2017. Among all these monitoring sites, Dianshanhu (DSH) is part of the rural region of Shanghai. The other four sites, Pudong (PD), Changzhou (CZ), Zhaohui (ZH) and Mingzhu (MZ), are categorized into urban sites, and they are in Shanghai, Jiangsu, Zhejiang and Anhui, respectively. We show the descriptions of these sites in Table S2 and Fig. 1. The offline measured aerosol chemical compositions include ions (SO_4^{2-}, NO_3^- and NH_4^+) and carbonaceous particles (OC and EC). To distinguish primary OC (POC) and secondary OC (SOC) from measurements, the EC-tracer method was adopted for further identification. The EC-tracer method assumes that the minimized ratio of OC to EC can indicate the primary compositions of organic matter (Ge et al., 2017), as shown in Eq. 7–8:

$$POC = EC \times \left(\frac{OC}{EC}\right)_{pri} \quad (7)$$

$$SOC = OC - POC \quad (8)$$

where $\left(\frac{OC}{EC}\right)_{pri}$ is the ratio of POC to EC. This ratio is roughly determined by the minimum OC to EC. In addition, an empirical value of 1.4 was applied to convert OC to OA (Ge et al., 2017).

3. Model evaluation

To describe the model performance in predicting meteorological parameters and chemical species, three statistical metrics were employed, including index of agreement (IOA, varies from 0 to 1), normalized mean bias (NMB, varies from –100 % to +∞) and root-mean-square error (RMSE, varies from 0 to +∞). Equations for IOA, NMB and RMSE are given in Eq. 9–11:

$$IOA = 1 - \frac{\sum_{i=1}^{N}(C_S - C_o)^2}{\sum_{i=1}^{N}(|C_S - \overline{C_o}| + |C_o - \overline{C_o}|)^2} \quad (9)$$

$$NMB = \frac{\sum_{i=1}^{N}(C_S - C_o)}{\sum_{i=1}^{N} C_o} \quad (10)$$

$$RMSE = \sqrt{\frac{\sum_{i=1}^{N}(C_S - C_o)^2}{N}} \quad (11)$$

where C is the concentration and N denotes the number of valid samples. Subscripts s and o represent the simulation and observation, respectively. Table 1 summarizes a comprehensive evaluation of the WRF-Chem model in terms of meteorological parameters, air pollutants and aerosol compositions.

3.1. Meteorological parameters and air pollutants

First, we validated the simulated meteorological parameters based on the four stations in the YRD region. A reliable simulation of meteorological fields is essential to successfully reproduce the advection and diffusion of the real atmosphere. The meteorological conditions simulated by WRF-Chem are generally eligible. In terms of magnitudes, the results show that the simulated temperature, RH and wind speed are 17.8 °C, 63.7 % and 3.5 m s^{-1}, respectively. They are close to the observed levels (18.4 °C, 70.1 % and 2.6 m s^{-1}). Moreover, NMB indicates that the WRF-Chem model has a bias from 3 % (temperature) to 37 % (wind speed). For temporal variations, the IOA values of these three meteorological parameters are 0.95, 0.74 and 0.58, emphasizing that WRF-Chem could capture the variations in meteorological fields. Especially for temperature, its IOA is close to 1. The detailed time series comparisons between observation versus simulation are also shown in Fig. S2.

The evaluation of six criteria air pollutants over the YRD region shows a good outcome (Table 1). The $PM_{2.5}$ simulation meets the criteria suggested by air quality model benchmarks (Huang et al., 2021), where IOA should be more than 0.70 and NMB should be less than ± 20 % (Table S8). As shown in Fig. 2, hourly variations in $PM_{2.5}$ concentrations are well captured by WRF-Chem in 26 cities of the YRD region, with a range of IOA from 0.59 (Wuhu) to 0.77 (Yangzhou and Chizhou). At the same time, 20 among 26 cities exceeded the recommended criteria of $PM_{2.5}$ simulation in terms of IOA.

Moreover, the reasonable spatial distribution pattern is also successfully reproduced by WRF-Chem. We showed comparisons between the simulations and observations of the spatial distributions of air pollutants in Fig. 2 and Fig. S3. Spatial correlations of these pollutants are universally positive, with the correlation coefficient ranging from 0.37 (O_3) to 0.85 ($PM_{2.5}$). Among all six criteria for air pollutants, the model predicts the spatial distribution of $PM_{2.5}$ the best. The simulated spatial distribution of $PM_{2.5}$ is close to the observed distribution (Fig. 2 a-b). In addition, the scatter plot demonstrates that the simulation is strongly correlated with the observation (r = 0.85). All dots are distributed around the 1:1 line, with a fitted slope of 1.2. This finding also implies that there is a strong agreement between the observations and the model in the spatial distribution of $PM_{2.5}$ (Fig. 2c). In general, although not without biases, our model showed a reasonable agreement with the surface observations in the YRD region, which allowed a decent evaluation of environmental and health effects of the Clean Air Plan.

3.2. Aerosol compositions

Apart from successfully capturing the routine $PM_{2.5}$ concentrations, the WRF-Chem model also reproduces the evolution of aerosol compositions, including SO_4^{2-}, NO_3^-, NH_4^+, EC and OA. Comparisons between observations and simulations of hourly concentrations at each site are provided in Fig. S4 and Fig. S5. We also show a comparison of the means across the five sites in Fig. 3. In general, the IOAs of SO_4^{2-}, NO_3^-, NH_4^+, EC and OA are 0.69, 0.64, 0.71, 0.62 and 0.58, respectively (Table 1). The corresponding NMBs are –16 %, 18 %, –11 %, –45 % and –1%, respectively. All aerosol compositions meet the criteria of recommendations for benchmarks except for EC (Table S8). The underestimation in terms of EC concentrations could be attributed to the biases of the emission inventory. Moreover, we evaluated the simulated POA and SOA based on the observation derived from the EC-tracer method (Fig. S6). The comparison indicates that POA is underestimated by 40 %. The underestimation is more obvious especially in April and July. For SOA, the revised WRF-Chem model can generally capture the concentration level.

Table 1
Comparison between simulation and observation results.

		Mean concentration		Metrics		
		Observation	Simulation	IOA	NMB	RMSE
Meteorological parameters	Temperature (℃)	18.4	17.8	0.95	−3%	2.8
	RH (%)	70.1	63.7	0.74	−9%	15.4
	Wind speed (m s^{-1})	2.6	3.5	0.58	37 %	1.9
Air pollutants	$PM_{2.5}$ (μg·m^{-3})	42.3	40.5	0.71	−4%	29.0
	8 h-O_3 (μg·m^{-3})	104.9	104.3	0.73	−1%	44.1
	NO_2 (μg·m^{-3})	36.0	28.7	0.70	−20 %	22.6
	CO (mg·m^{-3})	0.8	0.6	0.64	−31 %	0.4
	SO_2 (μg·m^{-3})	14.5	14.1	0.63	−3%	12.0
	PM_{10} (μg·m^{-3})	70.7	53.6	0.67	−24 %	46.2
Aerosol species	SO_4^{2-} (μg·m^{-3})	7.2	6.1	0.69	−16 %	5.9
	NO_3^- (μg·m^{-3})	8.7	10.3	0.64	18 %	10.5
	NH_4^+ (μg·m^{-3})	5.7	5.1	0.71	−11 %	4.7
	EC (μg·m^{-3})	2.3	1.3	0.62	−45 %	1.9
	OA (μg·m^{-3})	10.5	10.4	0.58	−1%	9.0

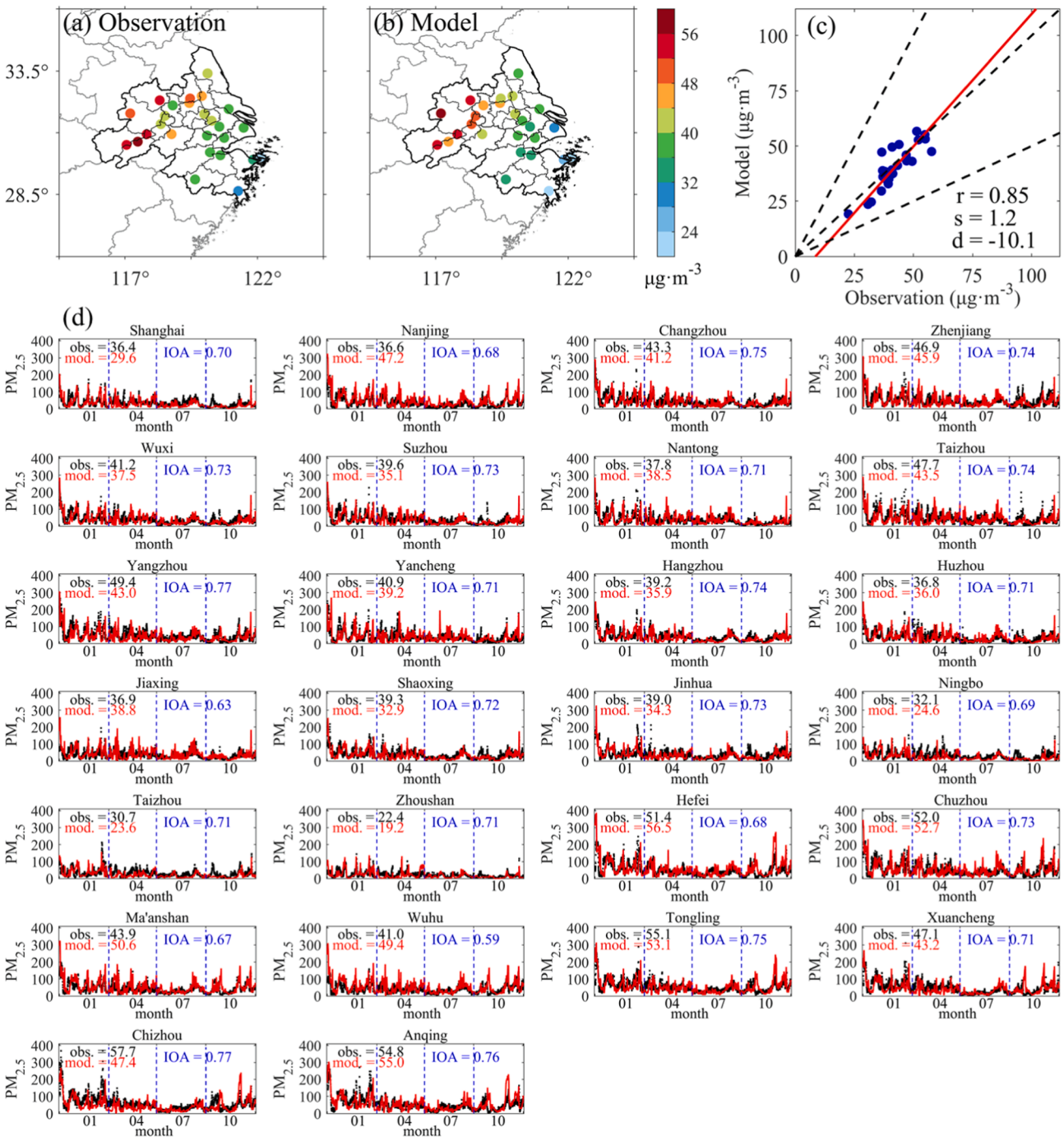

Fig. 2. Evaluation for $PM_{2.5}$ simulation in the YRD region during the study period. (a-b) Spatial distribution of the mean observation and simulation of $PM_{2.5}$ in 26 cities. In panel (c), a scatter plot is used for linear fitting between observation and simulation. Linear fitting is based on the reduced major axis (RMA) regression. Pearson correlation coefficient r as well as fitted metrics slope (s) and intercept (d) are marked at bottom right of panels. The black dotted line from left to right represents 2:1, 1:1 and 1:2 ratio respectively. (d) Detailed hourly comparisons between observed versus simulated $PM_{2.5}$ in 26 cities are also provided, where IOA, the average of observation and simulation are given in each city respectively.

However, our model sometimes may exhibit considerable over-estimation which is attributed to the uncertainties of VBS model.

In addition to considering the general characteristics of aerosol concentrations during the study period, this study also provides insights for investigating the features of specific aerosol pollution episodes. Here, we evaluate the model performance of SO_4^{2-} in winter haze events and SOA during the warm season after updating the aerosol mechanisms in WRF-Chem.

3.2.1. *Sulfate formation during the haze event*

We chose a four-day phase (12–15 Jan., marked as HZAE_JAN) to demonstrate the effect of this reaction on SO_4^{2-} formation. During this period, a haze event occurred on 12–13 January. The regional mean concentration of $PM_{2.5}$ is 87.9 $\mu g \cdot m^{-3}$, exceeding the level II ceiling of the National Ambient Air Quality Standard (NAAQS II, 75 $\mu g \cdot m^{-3}$). At the same time, we also show the observed temporal variations in SO_4^{2-} with the aid of in situ measurements in DSH, PD and CZ (Fig. 4 a-c). Measurements in ZH and MZ are unavailable for missing data.

The measured SO_4^{2-} concentration varied from 8.4 $\mu g \cdot m^{-3}$ (DSH) to

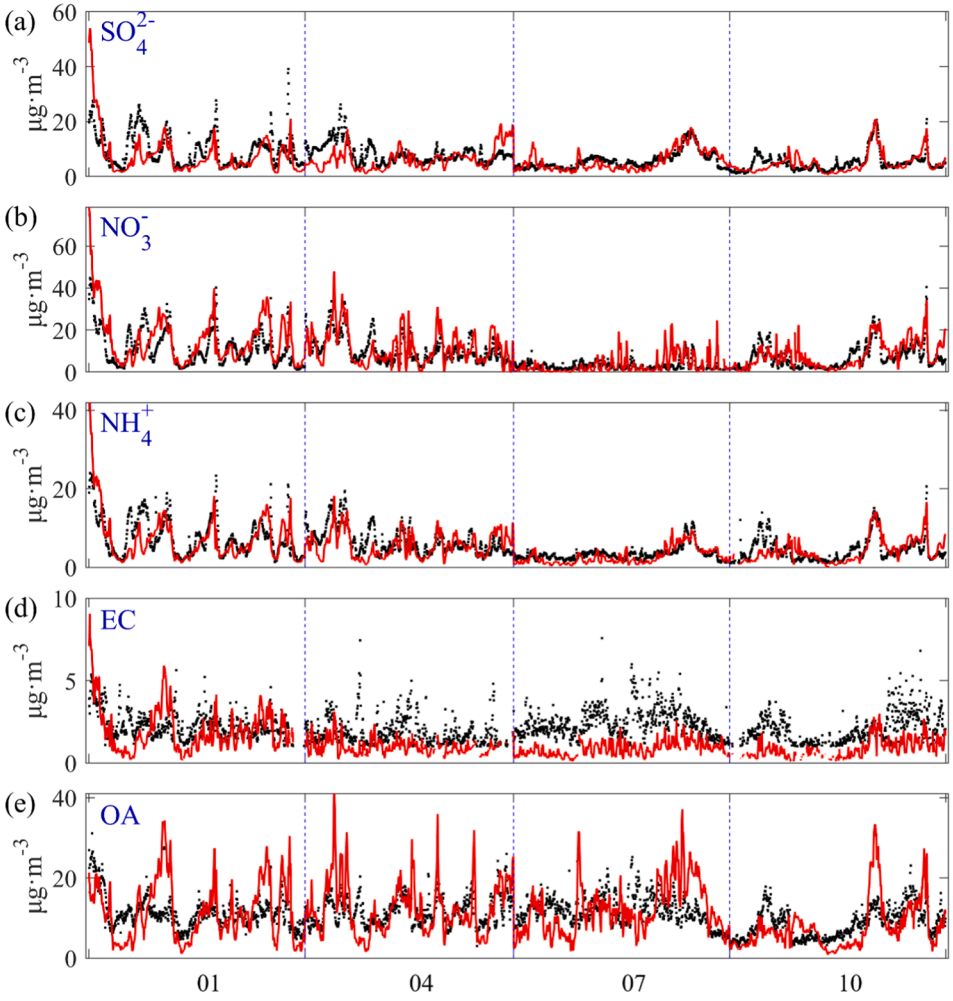

Fig. 3. Comparisons between mean observation versus mean simulation in terms of aerosol compositions, including (a) SO_4^{2-}, (b) NO_3^-, (c) NH_4^+, (d) EC and (e) OA. Mean of observation and simulation are labeled in black and red. IOA for each panel is labeled in blue.

10.2 μg·m^{-3} (CZ) on average during the HAZE_JAN period. The simulated SO_4^{2-} predicted by the standard model shows a massive underestimation in concentration level. The mean concentrations of the three sites during HAZE_JAN are 4.4–4.6 μg·m^{-3}, showing approximately –50 % in the NMB. The implementation of heterogeneous uptake helps to reduce the bias in simulating SO_4^{2-} concentrations. Generally, IOA and NMB improve by 16–23 % and 62–81 %, respectively, during HAZE_JAN. In particular, the updated reaction obviously increases the averaged SO_4^{2-} concentration of the three sites from 6.4 μg·m^{-3} to 12.7 μg·m^{-3} during 12–13 Jan., which is close to the observed value of 14.0 μg·m^{-3}. This increase may be less insignificant during the latter two days (January 14–15), with only a 0.3 μg·m^{-3} difference in mass concentration. The distinctive effects of the heterogenous reaction are attributed to the higher aerosol level during the haze event. Based on WRF-Chem, we find that the aerosol number concentration during the first two days is 48 % higher than that during the latter two days over the YRD region. Fig. 4d-f indicates that the heterogeneous uptake reaction can improve the concentration of simulated SO_4^{2-} spatially. The regional increase in SO_4^{2-} concentration due to this reaction is 3.2 μg·m^{-3}, which is approximately 70 % of the predicted concentration level of the standard WRF-Chem. On a monthly mean scale, implementing heterogenous uptake pathway increased the averaged SO_4^{2-} from 5.9 μg·m^{-3} to 7.4 μg·m^{-3}, with a relative increase of 25 %. The measured concentration level of SO_4^{2-} is 10.2 μg·m^{-3}. Meanwhile, the underestimation is well reduced from −42 % to −27 %.

3.2.2. SOA pollution in the warm season

S/IV-SOA and aq-SOA are two major causes of high SOA concentrations in the warm season. Here, we analysed the characteristics of SOA pollution during 3–24 July (marked as SOA_JUL) with the aid of in situ measurements in DSH, PD and MZ (Fig. 5). Observations at the other two sites are unavailable due to a lack of data. Based on the offline in situ measurements of the OC and EC-tracer models, the maximum measured SOA is above ~ 20 μg·m^{-3} during the warm season, and the mean observed concentration is 7.8 μg·m^{-3}. A routine model framework that only considers the oxidation of VOCs may greatly underestimate the SOA concentration by 74–79 % (Fig. S7). The application of the VBS framework in S/IVOCs as well as the implementation of aqueous uptake of GLY and MGLY can bridge this gap. However, the revised model may considerably overestimate the SOA concentration in the MZ by 65 %, which is mainly attributed to the overestimation of S/IV-SOA. The assumed emission factors and ageing parameters of S/IVOCs contain uncertainties (Matsui et al., 2014), and they may not be suitable for simulating the local evolution of SOAs in the MZ. Without regard to the MZ, the mean simulated SOA concentration was 8.9 μg·m^{-3}, successfully capturing the magnitude of the observed concentration level (7.9 μg·m^{-3}). In general, SOA is mainly contributed by S/IV-SOA during the SOA_JUL, with a fraction of 38–50 %. Aq-SOA accounted for 34–42 % of SOA during the SOA_JUL, among which mgly-SOA was approximately-two times higher than gly-SOA at all three sites. On a monthly mean scale, adding VBS framework increased the averaged SOA from 1.8 μg·m^{-3} to 10.6 μg·m^{-3}, with the measured concentration value of 7.8

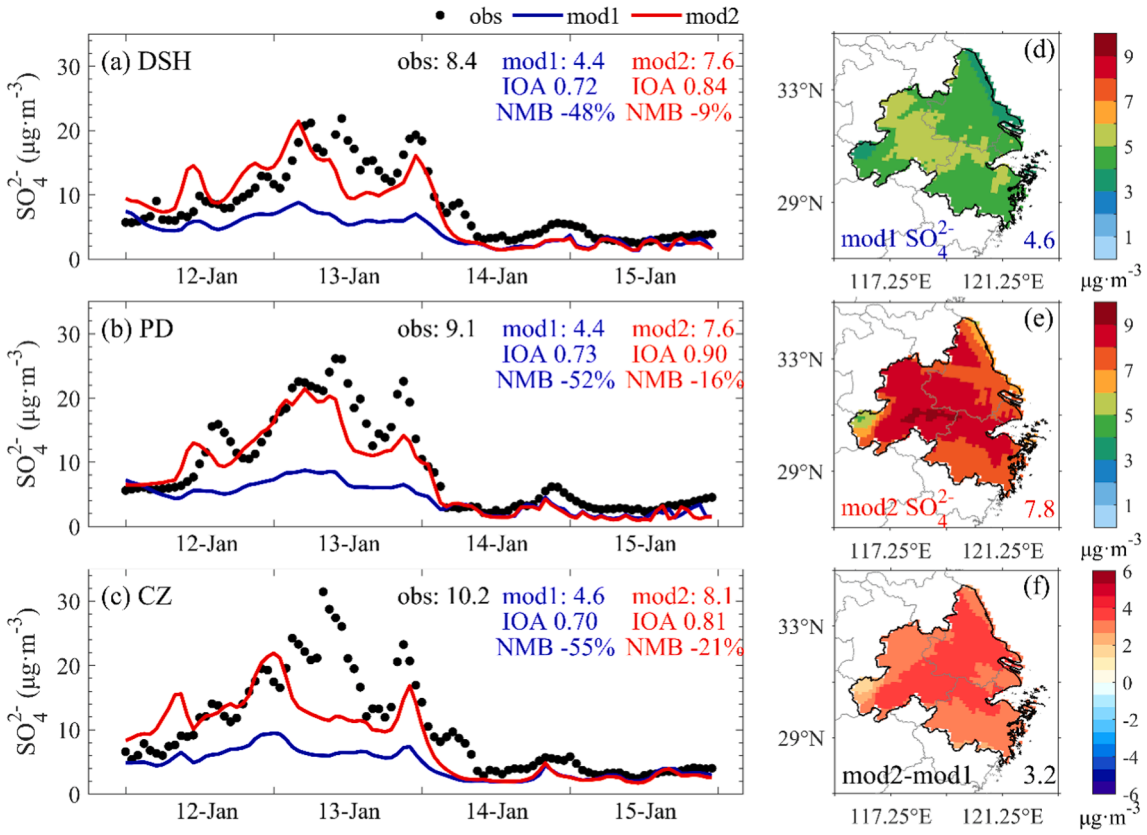

Fig. 4. Spatio-temporal variations of the simulated SO_4^{2-} during 12–15 Jan. Panels (a-c) show the temporal variation of observation (obs) versus simulation (mod1 and mod2) SO_4^{2-} in DSH, PD and CZ. The simulated mod1 means the SO_4^{2-} simulation based on the standard WRF-Chem. The simulated mod2 indicates the SO_4^{2-} simulation of the revised WRF-Chem which including heterogenous uptake of SO_4^{2-}. The related statistics such as the mean value, IOA and NMB are labeled in each panel. Spatial distribution of mod1 and mod2 SO_4^{2-}, as well as their difference (mod2 – mod1) are shown in panels (d-f).

$\mu g \cdot m^{-3}$. At the same time, the bias is improved from −77 % to + 36 %.

4. Characteristics of $PM_{2.5}$ pollution in 2017

After assessing the model performance, spatiotemporal characteristics of aerosol composition concentrations are analysed based on the WRF-Chem simulation across the YRD region in 2017.

4.1. Spatial distribution

In terms of spatial distribution, each aerosol composition as well as total $PM_{2.5}$ shows the same pattern. As shown in Fig. S8, aerosol concentrations are higher in the western YRD region and lower in the southeastern coastal areas. Taking $PM_{2.5}$ as an example, its average concentration exceeds 50 $\mu g \cdot m^{-3}$ in the western YRD region. However, the regional minimum is only ~ 20 $\mu g \cdot m^{-3}$ in the southeastern YRD. Thus, there is an obvious gradient of aerosol concentrations that exist from inland to the ocean with a declining tendency. The intensive emissions in the inland YRD region and the sea breeze led to the spatial distribution differences in aerosol concentrations. The aerosol composition for each province in the YRD is illustrated in Fig. S9. The simulated concentrations indicate that the aerosol concentration in Anhui is the highest (47.6 $\mu g \cdot m^{-3}$), followed by that in Jiangsu (38.4 $\mu g \cdot m^{-3}$), Shanghai (29.9 $\mu g \cdot m^{-3}$) and Zhejiang (29.3 $\mu g \cdot m^{-3}$). Although the magnitudes of $PM_{2.5}$ concentrations exhibit a clear discrepancy, the characteristics of aerosol compositions tend to be consistent in all four provinces.

4.2. Seasonal variations

The simulated aerosols also exhibit different seasonal variation characteristics. The seasonal features of $PM_{2.5}$ and its components in the YRD region during the study period are shown in Fig. 6. The seasonal mean $PM_{2.5}$ concentrations are 53.9 $\mu g \cdot m^{-3}$, 35.4 $\mu g \cdot m^{-3}$, 27.6 $\mu g \cdot m^{-3}$ and 29.8 $\mu g \cdot m^{-3}$ in winter, spring, summer and fall, respectively. In general, $PM_{2.5}$ is higher in winter and lower in summer. Seasonal differences are mainly dominated by the variable meteorological effects. For example, high planetary boundary layer height (PBLH), abundant precipitation and monsoons coming from the southeast ocean in summer are helpful for the removal of aerosols. The unfavourable causes of stagnant $PM_{2.5}$ include the stable circulation pattern and inversion layer in winter.

$PM_{2.5}$ shows different chemical compositions in different seasons. In terms of primary $PM_{2.5}$ (including POA, EC, dust and sea salt), its concentration varies from 5.5 $\mu g \cdot m^{-3}$ (summer) to 14.3 $\mu g \cdot m^{-3}$ (winter). The relative fraction of primary $PM_{2.5}$ among the total $PM_{2.5}$ ranges from 17 % (spring) to 26 % (winter). Dust is the dominant component of primary $PM_{2.5}$, with a contribution of 57–74 % to primary $PM_{2.5}$ concentration. Concentrations of primary carbonaceous aerosols (EC and POA) are higher in winter and spring (2.6–5.7 $\mu g \cdot m^{-3}$). However, higher dust concentrations occur in winter and fall (5.2–8.6 $\mu g \cdot m^{-3}$).

Concentrations of SO_4^{2-}, NO_3^- and NH_4^+ show the same seasonal patterns, with higher concentrations in winter and lower concentrations in summer. Among secondary PM, NO_3^- contributes to nearly half of the SNA concentration, accounting for approximately 28 % of the $PM_{2.5}$ concentration. However, the dominant component of SNA changes from NO_3^- to SO_4^{2-} in summer. The relative contribution of NO_3^- to $PM_{2.5}$ composition drops from 27 to 28 % in nonsummer seasons to 15 % in

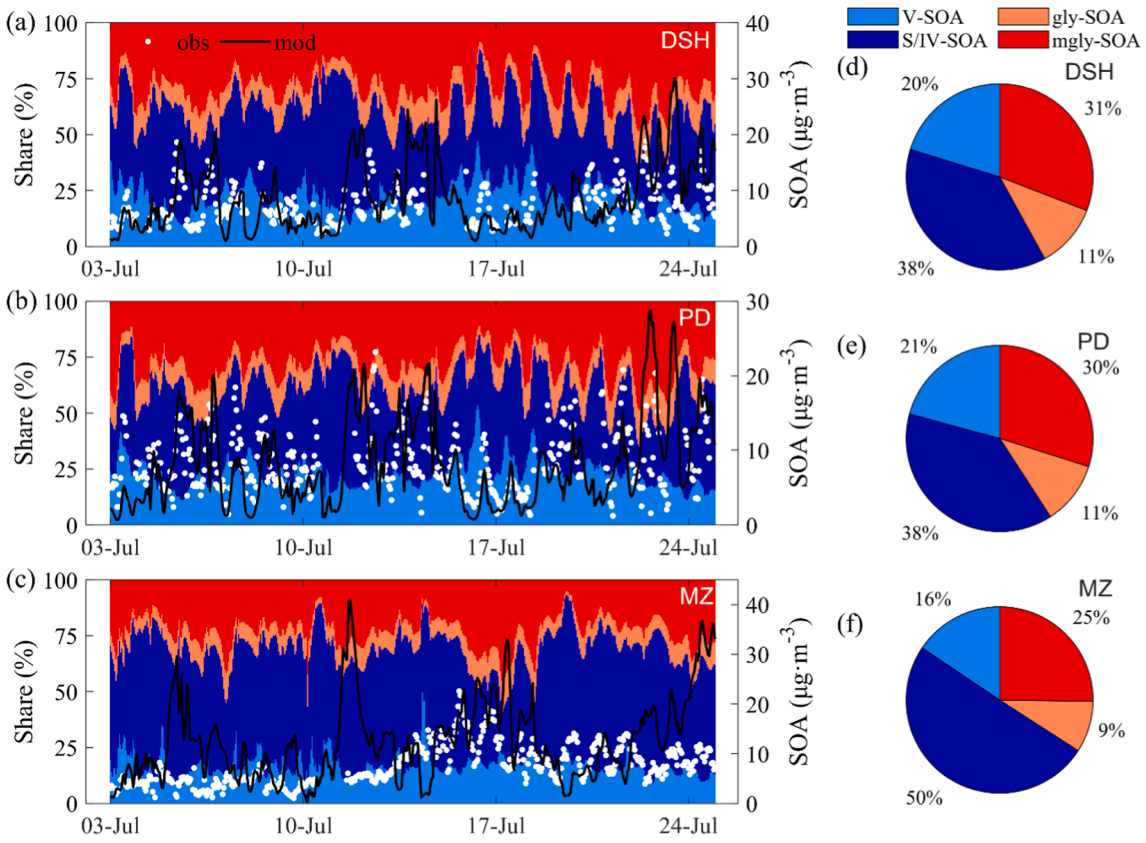

Fig. 5. Spatio-temporal variations of the simulated SOA during 3–24 July. Panels (a-c) indicate the simulated SOA (mod, black lines) as well as the observed ones (obs, white dots) in DSH, PD and MZ. The contribution of each composition among SOA is also shown, including V-SOA, S/IV-SOA, gly-SOA and mgly-SOA. The averaged compositions of SOA during this period in three sites are provided in panels (d-f).

summer. This change could be explained by the following two reasons. One reason is the evaporation of NH_4NO_3 under high ambient temperatures in summer (Dawson et al., 2007). The other cause is the competition between HNO_4 and H_2SO_4 for gaseous ammonia. Based on the diagnostic indicator particle neutralization ratio (PNR, Eq.12), which is defined as the mole ratio of total NH_4^+ to net NO_3^- and SO_4^{2-} (Yin et al., 2018), the YRD region is expected to be ammonia-poor, consistent with Pathak et al. (2011) and Pathak et al. (2009). Thus, the YRD region experiences strong atmospheric oxidation capacity (AOC) and the limited ammonia would collectively suppress the production of NO_3^- in summer.

$$PNR = \frac{n[NH_4^+]}{2n[SO_4^{2-}] + n[NO_3^-]} \qquad (12)$$

In contrast, SOA exhibits the opposite pattern in seasonal variation. The SOA concentrations are higher in summer and spring (9.0–9.5 $\mu g \cdot m^{-3}$) and lower in fall and winter (5.7–8.1 $\mu g \cdot m^{-3}$). The seasonal peak during the summertime allowed SOA to be the dominant aerosol composition, contributing 35 % to the total $PM_{2.5}$ concentration. To further clarify the contributions of various sources to SOA formation, we illustrate the compositions of SOA in different seasons in Fig. 7. We name SOAs that evolve from VOCs, S/IVOCs, GLY and MGLY V-SOA, S/IV-SOA, gly-SOA and mgly-SOA, respectively. The largest source of SOA is the oxidation and ageing of S/IVOCs, with a 45–64 % contribution to SOA and a 33–54 % contribution to OA. In addition, aq-SOA occupies a considerable proportion of OA as well, ranging from 21 % (spring) to 34 % (summer), which is comparable to previous results in China (Li et al., 2013; Ling et al., 2020; Xing et al., 2019). Within dicarbonyl, MGLY leads to more aq-SOA, where mgly-SOA is 65 % of the total aq-SOA concentration on average. V-SOA, which is produced via traditional oxidation, only explains 5–14 % of the OA concentration.

Both maxima of V-SOA and aq-SOA concentrations occur in the summertime, with the associated seasonal peaks of 1.5 $\mu g \cdot m^{-3}$ and 3.7 $\mu g \cdot m^{-3}$, respectively. The higher concentrations of their precursors result in the seasonal peak in summer (Table S9). Moreover, the higher humidity in the summertime also provides enough vapour for aqueous reactions. However, the seasonal mean concentration of aq-SOA is also high (3.6 $\mu g \cdot m^{-3}$) in winter, which could be ascribed to the enhanced surface uptake of dicarbonyl due to the larger aerosol surface areas supplied by high $PM_{2.5}$ loading. In conclusion, the simulated OA showed that more than 80 % of the concentrations were secondarily generated except in winter. Moreover, in Section 5.2, we also analyse the detailed compositions of SOA during the warm season compared with the in situ measurements.

4.3. Diurnal variations

Diurnal variations in various aerosol compositions exhibit different patterns. Fig. S9a illustrates the diurnal variations in SNA, SOA and primary $PM_{2.5}$. The diurnal pattern of primary $PM_{2.5}$ is mainly influenced by the local emission levels and the PBLH. PBLH reflects the efficiency of vertical diffusion (Fig. S9b). The intensive emissions due to traffic transportation in the presence of the lower PBLH (~400 m) contribute to two peaks in primary $PM_{2.5}$ at approximately 7:00 and 21:00. Although both SNA and SOA are secondary products of oxidized reactions, their diurnal variations show discrepancies. The diurnal peak in SOA concentration (8.8 $\mu g \cdot m^{-3}$) occurs at ~ 15:00 because AOC is extremely strengthened by then. As an indicator of AOC, O_3 demonstrates the same pattern as SOA in its diurnal variation. Moreover, the biogenic emissions that are the most active over the same period also provide precursors to SOA formation. In contrast, SNA reaches the minimum at 15:00 but stays at a high concentration level during the

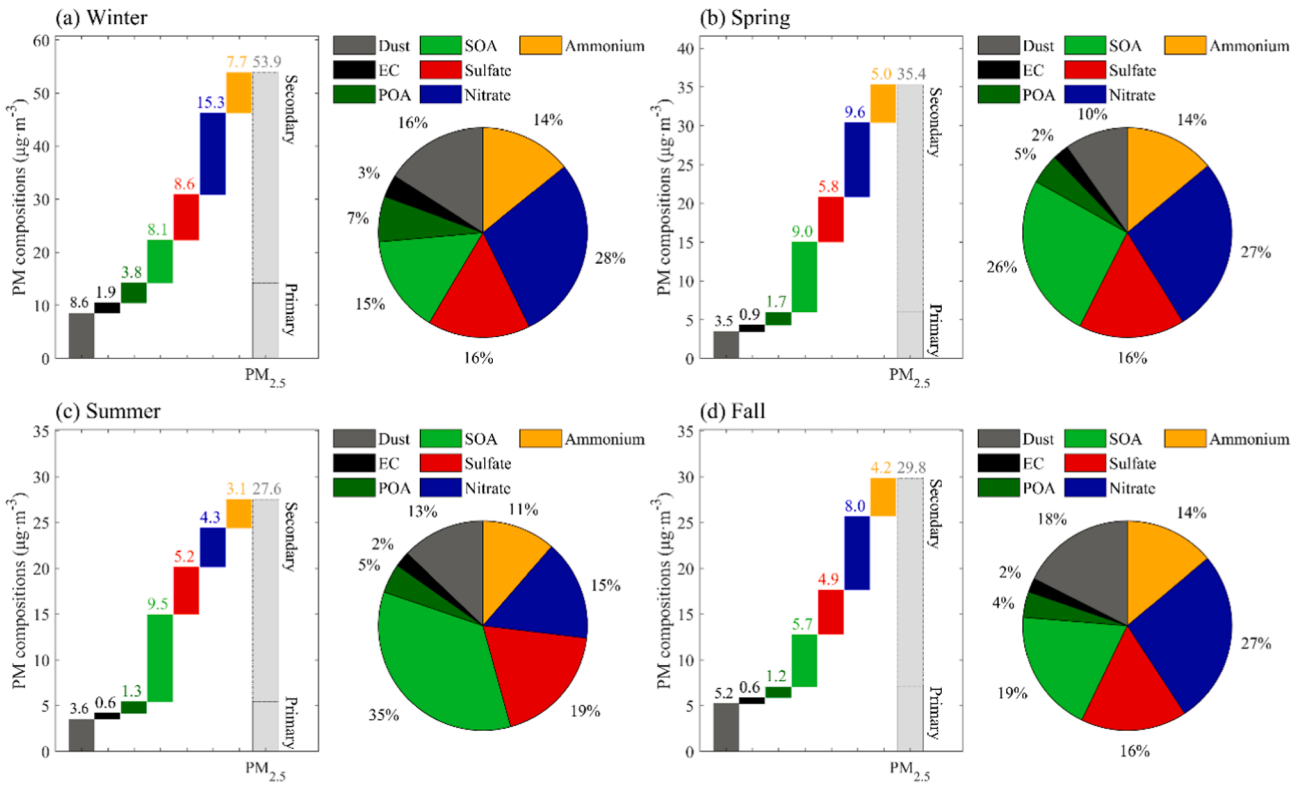

Fig. 6. Seasonal variations of aerosol chemical compositions in the YRD region. Panels (a-d) means January, April, July and October in 2017. Waterfall plot in each panel indicates the concentrations of various aerosol species. Pie plot shows the relative shares of chemical components among total $PM_{2.5}$ concentrations. Value of each colored diagram is labeled at the nearby area.

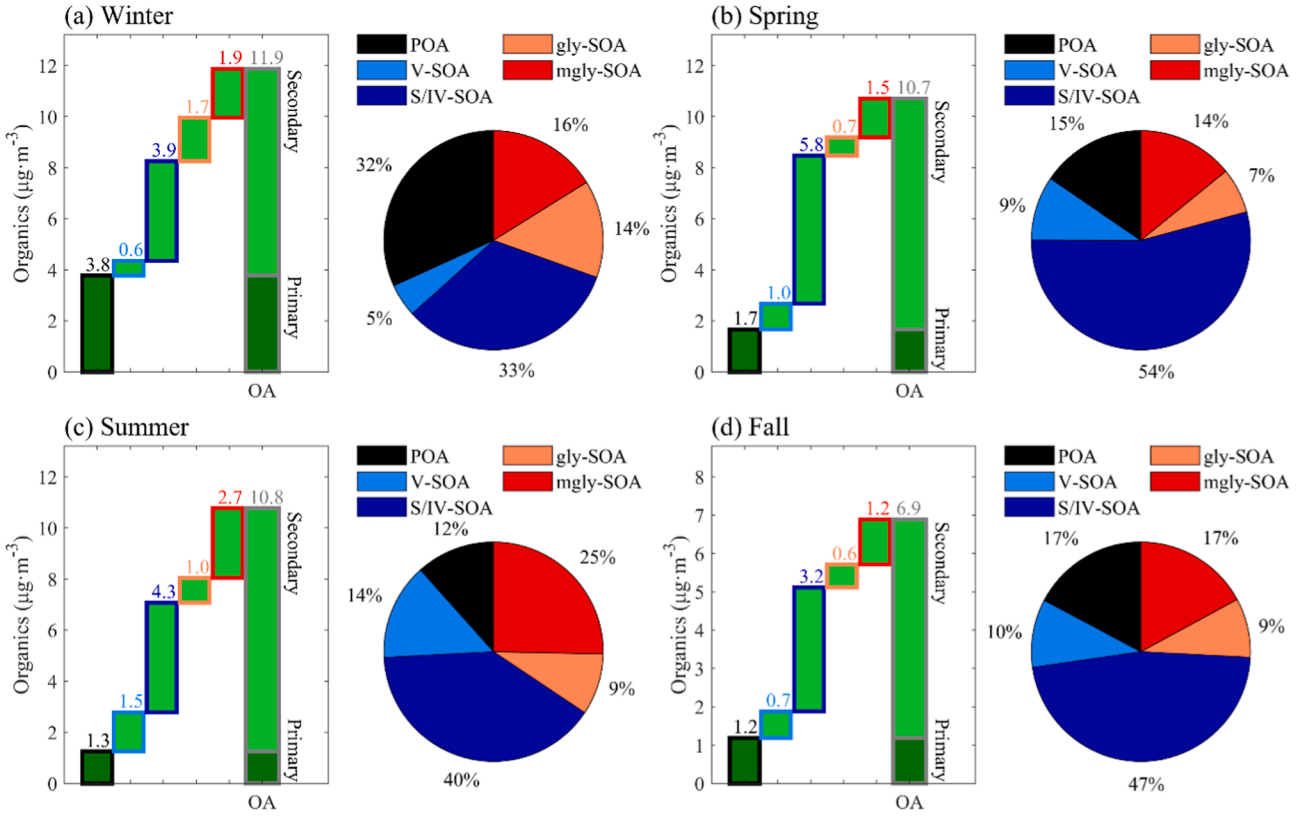

Fig. 7. The same as Fig. 6, but for organic aerosols.

nighttime (0:00–5:00). This phenomenon could be mostly explained by the effect of PBLH. For the peaks of SNA at night, the production of nitrate particles via N_2O_5 radicals could also be a potential cause.

4.4. Premature mortality analysis

$GEMM_{NCD+LRI}$ model highlights that $PM_{2.5}$ exposure induces several hundreds of thousands of premature mortalities over the YRD region in 2017. As listed in Table S10, the number of premature mortalities is largest in Jiangsu (114.1 thousand, 95 %CI: 43.1–186.3), followed by Zhejiang (67.2 thousand, 95 %CI: 30.3–130.8), Anhui (65.0 thousand, 95 %CI: 21.1–91.4) and Shanghai (49.5 thousand, 95 %CI: 22.5–97.1). Given the population of each province, the per capita mortalities in Shanghai, Jiangsu and Anhui are 20.6 (95 %CI: 9.4–40.5), 21.5 (95 %CI: 8.1–35.1) and 21.7 (95 %CI: 7.0–30.5) per 10 thousand persons, respectively, but they are significantly lower in Zhejiang (16.9, 95 %CI: 7.6–32.9), which can be explained by its lower levels of $PM_{2.5}$ pollution. We show the spatial distribution of premature mortality in Fig. 8. Most premature mortalities occur in densely populated areas, such as Shanghai and southern Jiangsu. This spatial distribution pattern of premature mortality is different from that of $PM_{2.5}$ mass concentration. In terms of premature mortality among different ages, the number of deaths exponentially increases. Generally, people over 60 years old make up 88 % of total premature mortality in the YRD region. The most harmful cause of death is NCD + LRI, which induces 52 % of total premature mortality, and IHD ranks second, contributing 17 %. Compared to other causes of death, NCD + LRI has the higher baseline mortality rate.

IER model estimates 146.8 (95 %CI: 31.0–217.9) thousand deaths in the YRD region, which weighs 50 % of the $GEMM_{NCD+LRI}$ result. The ratio of IER to $GEMM_{NCD+LRI}$ in this study is in agreement with those in previous studies (Burnett et al., 2018; Dang and Liao, 2019; Maji, 2020; Wu et al., 2021; Zhang et al., 2019; Ding D. et al., 2019). Zhang et al. (2019) found that premature death in the YRD region is 117.8 (IER) and 264.2 ($GEMM_{NCD+LRI}$) thousand in 2017, which is close to our estimate. Ding D. et al. (2019) calculated that the number of deaths in Shanghai in 2017 based on IER model is 19.7 thousand, approximately 22 % lower than our estimate. The differences are mainly attributed to the discrepancies of $PM_{2.5}$ estimation. The simulated $PM_{2.5}$ spatial patterns may result in considerable uncertainties of $PM_{2.5}$ exposure for populations.

5. Effects of the Clean air Plan on $PM_{2.5}$ pollution and the associated health benefits

With the aid of the updated WRF-Chem model, we assessed the alleviation of $PM_{2.5}$ concentrations and its related premature mortalities due to the emission reduction effects of the Clean Air Plan in the YRD region. The sensitivity experiment quantifies that the total $PM_{2.5}$ concentration decreases by 33 % compared to the pollution level in 2013 (Fig. 8c and Fig. 9a). In spatial patterns, the concentration reductions of $PM_{2.5}$ mainly take place around the Yangtze River, with the regional maximum reduction exceeding 40 $\mu g \cdot m^{-3}$. Within various $PM_{2.5}$ compositions, primary $PM_{2.5}$ (including dust, EC and POA) decreased most significantly (55–61 %) during 2013–2017, which indicates that the Clean Air Plan has a series of effective measures for eliminating primary $PM_{2.5}$ emissions, especially for flying dust (decreased by 6.5 $\mu g \cdot m^{-3}$). For secondary aerosols, SNA and SOA decreased by 4.3 $\mu g \cdot m^{-3}$ and 3.4 $\mu g \cdot m^{-3}$, respectively. In terms of SNA, the model results show that the relative declines in SO_4^{2-} and NO_3^- are 24 % and 12 %, respectively, mainly benefiting from the reduction in ambient SO_2 (50 %) and NO_2 (24 %). For SOA, its drop is mostly explained by the decrease in S/IVOCs. SOA acting as the dominant composition of SOA. The drop in S/IVOCs results from the simultaneous decline in S/IVOCs, which largely benefits from the reduced POA emissions. The decreasing but variable trends of primary and secondary particles also led to the change in aerosol composition pattern. In general, the $PM_{2.5}$ pollution in the YRD region is transforming into a secondary dominated stage. Especially for NO_3^-, its fraction of $PM_{2.5}$ rises from 19 % to 25 % because of the mitigative effect of the Clean Air Plan.

Based on the $GEMM_{NCD+LRI}$ results of ANTH_13, the premature mortality per capita caused by $PM_{2.5}$ in Shanghai, Jiangsu, Zhejiang and

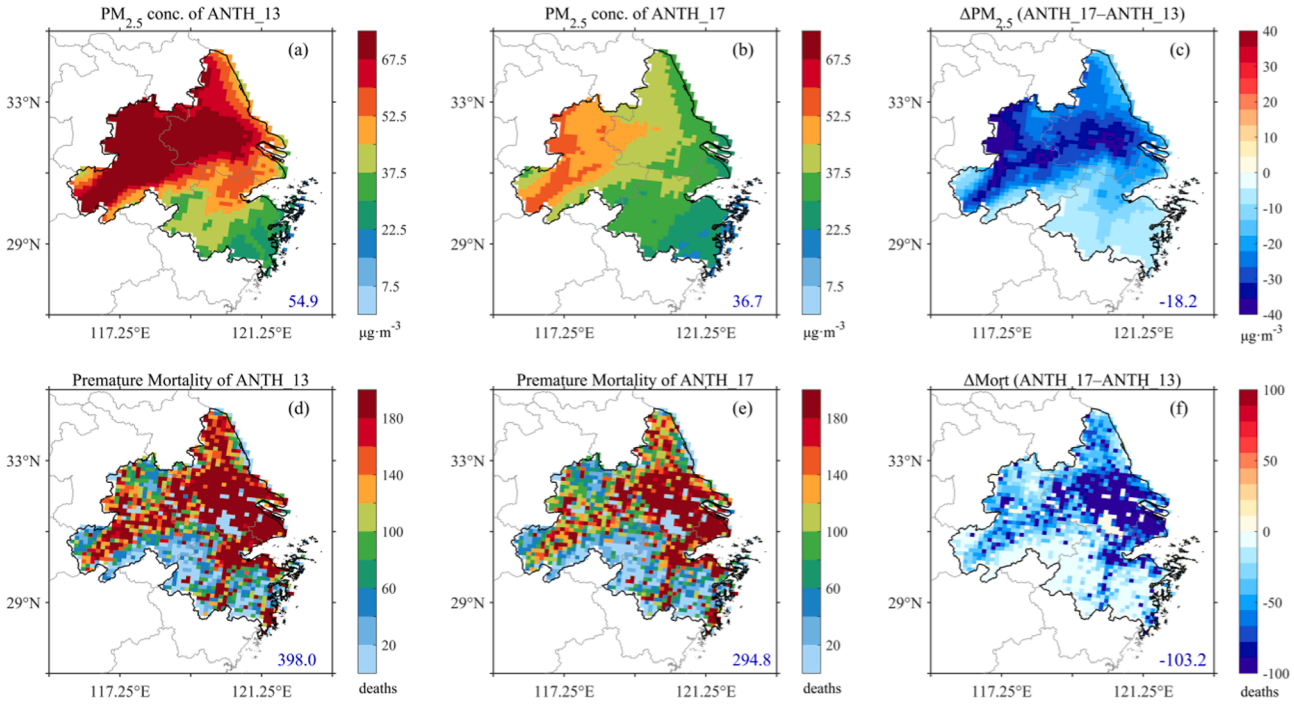

Fig. 8. Spatial distributions of reductions in $PM_{2.5}$ concentration (a-c) and premature mortality (d-f). The blue numbers labeled in the panels a-c denote the regional mean concentration of $PM_{2.5}$ as well as its reduction (Unit: $\mu g \cdot m^{-3}$). However, these blue numbers labeled in the panels d-f stand for the regional total premature death as well as its reduction (Unit: 1 thousand people).

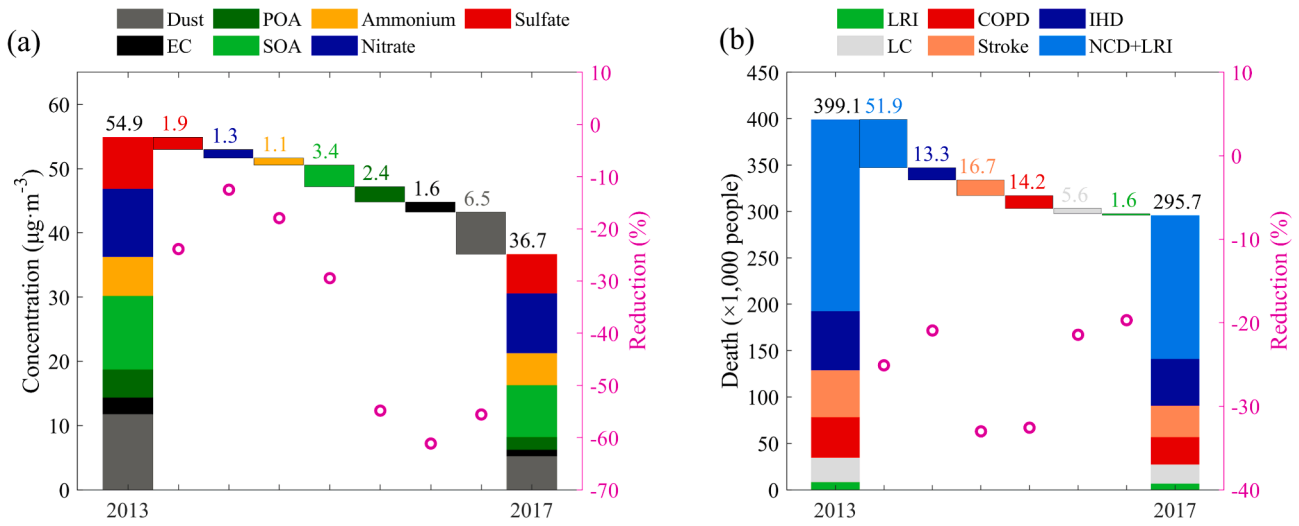

Fig. 9. Comparisons between ANTN_13 versus ANTH_17 in (a) $PM_{2.5}$ compositions and (b) premature death caused by different diseases. Values above the bars indicate the reductions of the corresponding concentrations and numbers of premature mortality. The relative declines are also shown by pink circles.

Anhui is 28.8 (95 % CI: 10.1–42.9), 30.8 (95 %CI: 9.0–38.5), 21.0 (95 % CI: 8.3–35.6) and 29.3 (95 %CI: 7.9–33.9) per 10 thousand persons, respectively (Table S11). The declines in $PM_{2.5}$ led to the associated drops in premature mortality by 17–27 % in the four provinces. Generally, the total premature mortality over the YRD region decreased from 399.1 (95 %CI: 127.4–543.9) thousand in 2013 to 295.7 (95 %CI: 117.0–505.6) thousand in 2017, with a relative decline by 26 %. As shown in Fig. 8d-f, the spatial distribution of ΔMort illustrates the same pattern as the estimated spatial distribution of premature mortality, where values are higher approaching the densely populated areas. Fig. 9b further demonstrates that the decreased premature deaths due to NCD + LRI, IHD, stroke, COPD, LC and LRI are 51.9, 13.3, 16.7, 14.2, 5.6 and 1.6 thousand, respectively, with relative declines ranging from 20 % (LRI) to 33 % (stroke). We further investigated the synergistic relationship between $PM_{2.5}$ concentration improvement and premature mortality reduction by means of linear fitting. As illustrated in Fig. 10, the regressions in all four provinces show high agreement, with R^2 ranging from 0.92 (Jiangsu) to 0.99 (Zhejiang). At the same time, the fitted formulas indicate that the benefit of every reduction by 1 $\mu g \cdot m^{-3}$ $PM_{2.5}$ concentration is most significant in Shanghai, with an approximately 3.17 per 10 thousand persons decrease in per capita mortality. However, this response to $PM_{2.5}$ concentration reduction is less effective in Anhui, with a decrease by 1.66 per 10 thousand persons in premature deaths in the presence of every 1 $\mu g \cdot m^{-3}$ reduction in $PM_{2.5}$. The difference of per capita mortality due to $PM_{2.5}$ reduction is attributed to both different $PM_{2.5}$ concentration level and diverse age groups in different YRD provinces.

6. Conclusions

In this study, we simulated aerosol pollution over the YRD region in 2017 with the aim of assessing the air quality improvement and its associated health burden in the final year of the Clean Air Plan. To better describe the fate of various $PM_{2.5}$ compositions, we first updated the aerosol module by implementing the heterogenous uptake of SO_4^{2-} and additional SOA reactions, including the VBS framework and the aqueous reactive uptake of GLY and MGLY. Moreover, various observations were collected to evaluate the model performance of both the total $PM_{2.5}$ concentrations and their compositions. A series of sensitivity simulations quantified that the annual mean $PM_{2.5}$ concentration in 2017 decreased by 33 % compared to 2013. Inconsistent decreasing trends of $PM_{2.5}$ components subsequently led to an increasing proportion of secondary $PM_{2.5}$, especially for NO_3^-, and its fraction of $PM_{2.5}$ rose from 19

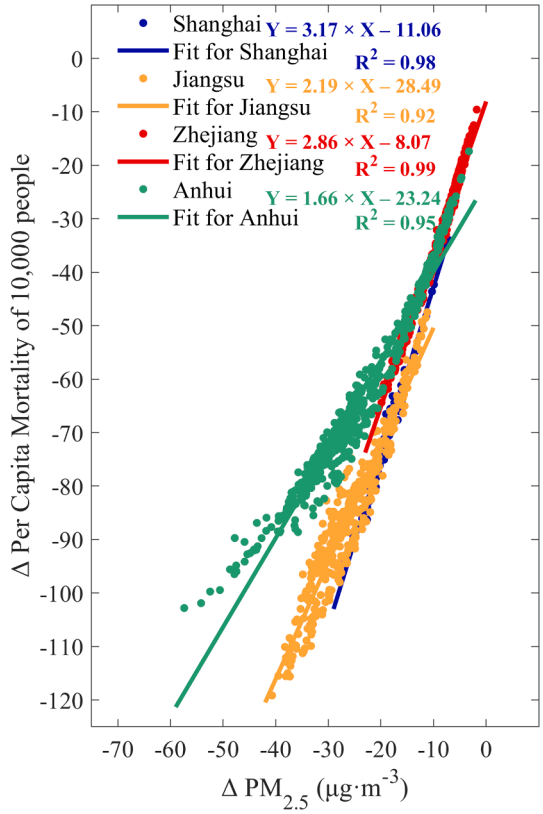

Fig. 10. The linear regression between $PM_{2.5}$ reduction ($\Delta PM_{2.5}$) versus per capita mortality reduction (ΔPCM) in four provinces. Each dot stands for a reduction in $PM_{2.5}$ and per capita mortality estimated in one grid cell. The fitted formulas and goodness of fit (R^2) are labeled in the lower left and right respectively.

% to 25 %. The regression analysis between $PM_{2.5}$ concentration improvement and per capita mortality reduction further shows a response of 1.66–3.17 per 10 thousand persons decrease in per capita mortality, with an R^2 of 0.92–0.99. China is undergoing a fast stage of mitigating $PM_{2.5}$. Our work merged multiple methods and data to provide comprehensive insights into the patterns of $PM_{2.5}$ pollution in 2017 and quantified the long-term mitigative benefits of $PM_{2.5}$ and the

associated premature mortality. This is crucial for policy-makers to further develop emission control strategies.

Data availability

The open-source codes of WRF-Chem model are available at UCAR official website (https://www2.mmm.ucar.edu/wrf/users/). Observation about air quality and chemical measurements and modeling results in main text are available upon request to the corresponding author (linan@nuist.edu.cn).

CRediT authorship contribution statement

Nan Li: Conceptualization, Funding acquisition, Resources, Writing – review & editing. **Haoran Zhang:** Conceptualization, Data curation, Formal analysis, Methodology, Visualization. **Shuhan Zhu:** . **Hong Liao:** Funding acquisition, Project administration, Supervision. **Jianlin Hu:** Data curation, Visualization. **Keqin Tang:** Data curation, Visualization. **Weihang Feng:** Data curation, Visualization. **Ruhan Zhang:** Data curation, Visualization. **Chong Shi:** Data curation, Visualization. **Hongmei Xu:** Data curation, Visualization. **Lei Chen:** Data curation, Visualization. **Jiandong Li:** Data curation, Visualization.

Declaration of Competing Interest

The authors declare that they have no known competing financial interests or personal relationships that could have appeared to influence the work reported in this paper.

Data availability

Data will be made available on request.

Acknowledgements

This work was supported by the National Key Research and Development Program of China (2019YFA0606804), the National Natural Science Foundation of China (41975171), the Natural Science Foundation of Jiangsu Province (Grant No. BK20220031), and the Major Research Plan of the National Social Science Foundation (18ZDA052). The numerical calculations in this paper have been done on the supercomputing system in the Supercomputing Center of Nanjing University of Information Science & Technology.

Appendix A. Supplementary material

Supplementary data to this article can be found online at https://doi.org/10.1016/j.envint.2022.107725.

References

An, Z.S., Huang, R.J., Zhang, R.Y., Tie, X.X., Li, G.H., Cao, J.J., Zhou, W.J., Shi, Z.G., Han, Y.G., Gu, Z.L., Ji, Y.M., 2019. Severe haze in northern China, a synergy of anthropogenic emissions and atmospheric processes. Proc. Natl. Acad. Sci. 116, 8657–8666.

An, J.Y., Huang, Y.W., Huang, C., Wang, X., Yan, R.S., Wang, Q., Wang, H.L., Jing, S.A., Zhang, Y., Liu, Y.M., Chen, Y., Xu, C., Qiao, L.P., Zhou, M., Zhu, S.H., Hu, Q.Y., Lu, J., Chen, C.H., 2021. Emission inventory of air pollutants and chemical speciation for specific anthropogenic sources based on local measurements in the Yangtze River Delta region. China. Atmos. Chem. Phys. 21, 2003–2025.

Burnett, R., Chen, H., Szyszkowicz, M., Fann, N., Hubbell, B., Pope 3rd, C.A., Apte, J.S., Brauer, M., Cohen, A., Weichenthal, S., Coggins, J., Di, Q., Brunekreef, B., Frostad, J., Lim, S.S., Kan, H., Walker, K.D., Thurston, G.D., Hayes, R.B., Lim, C.C., Turner, M.C., Jerrett, M., Krewski, D., Gapstur, S.M., Diver, W.R., Ostro, B., Goldberg, D., Crouse, D.L., Martin, R.V., Peters, P., Pinault, L., Tjepkema, M., van Donkelaar, A., Villeneuve, P.J., Miller, A.B., Yin, P., Zhou, M., Wang, L., Janssen, N. A.H., Marra, M., Atkinson, R.W., Tsang, H., Quoc Thach, T., Cannon, J.B., Allen, R. T., Hart, J.E., Laden, F., Cesaroni, G., Forastiere, F., Weinmayr, G., Jaensch, A., Nagel, G., Concin, H., Spadaro, J.V., 2018. Global estimates of mortality associated with long-term exposure to outdoor fine particulate matter. Proc. Natl. Acad. Sci. 115, 9592–9597.

Burnett, R.T., Pope, C.A., Ezzati, M., Olives, C., Lim, S.S., Mehta, S., Shin, H.H., Singh, G., Hubbell, B., Brauer, M., Anderson, H.R., Smith, K.R., Balmes, J.R., Bruce, N.G., Kan, H., Laden, F., Pruss-Ustun, A., Turner, M.C., Gapstur, S.M., Diver, W.R., Cohen, A., 2014. An integrated risk function for estimating the global burden of disease attributable to ambient fine particulate matter exposure. Environ. Health Perspect. 122, 397–403.

Carter, W.P.L., 2000. Documentation of the SAPRC-99 Chemical Mechanism for VOC Reactivity Assessment. Final Report to California Air Res. Board.

Chen, F., Dudhia, J., 2001. Coupling an Advanced Land Surfac-Hydrology Model with the Penn State-NCAR MM5 Modeling System. Part I, model implementation and sensitivity. Mon. Weather Rev. 129, 569–585.

Chen, L., Zhu, J., Liao, H., Yang, Y., Yue, X., 2020. Meteorological influences on $PM_{2.5}$ and O_3 trends and associated health burden since China's clean air actions. Sci. Total Environ. 744, 140837.

Cheng, Y.F., Zheng, G.J., Wei, C., Mu, Q., Zheng, B., Wang, Z.B., Gao, M., Zhang, Q., He, K., Carmichael, G., Poschl, U., 2016. Reactive nitrogen chemistry in aerosol water as a source of sulfate during haze events in China. Sci. Adv. 2, e1601530–e.

Chu, B.W., Ma, Q.X., Liu, J., Ma, J.Z., Zhang, P., Chen, T.Z., Feng, Q.C., Wang, C.Y., Yang, N., Ma, H.N., Ma, J.J., Russell, A.G., He, H., 2020. Air Pollutant correlations in china, secondary air pollutant responses to NO_x and SO_2 Control. Environ. Sci. & Technol. Lett. 7, 695–700.

Dang, R., Liao, H., Fu, Y., 2021. Quantifying the anthropogenic and meteorological influences on summertime surface ozone in China over 2012–2017. Sci. Total Environ. 754, 142394.

Dang, R.J., Liao, H., 2019. Radiative Forcing and Health Impact of Aerosols and Ozone in China as the Consequence of Clean Air Actions over 2012–2017. Geophys. Res. Lett. 46, 12511–12519.

Dawson, J.P., Adams, P.J., Pandis, S.N., 2007. Sensitivity of PM2.5 to climate in the Eastern US, a modeling case study. Atmos. Chem. Phys 7, 4295–4309.

D, Ding, J, Xing, S.X, Wang, K.Y, Liu, J.M, Hao, Estimated Contributions of Emissions Controls, Meteorological Factors, Population Growth, and Changes in Baseline Mortality to Reductions in Ambient $PM_{2.5}$ and $PM_{2.5}$-Related Mortality in China, 2013-2017. Environ. Health Perspect. 127 2019, 67009.

Ding, A.J., Huang, X., Nie, W., Chi, X.G., Xu, Z., Zheng, L.F., Xu, Z.N., Xie, Y.N., Qi, X.M., Shen, Y.C., Sun, P., Wang, J.P., Wang, L., Sun, J.N., Yang, X.-Q., Qin, W., Zhang, X. Z., Cheng, W., Liu, W.J., Pan, L.B., Fu, C.B., 2019a. Significant reduction of PM2.5 in eastern China due to regional-scale emission control, evidence from SORPES in 2011–2018. Atmos. Chem. Phys. 19, 11791–11801.

Elser, M., Huang, R.J., Wolf, R., Slowik, J.G., Wang, Q., Canonaco, F., Li, G.H., Bozzetti, C., Daellenbach, K.R., Huang, Y., Zhang, R.J., Li, Z.Q., Cao, J.J., Baltensperger, U., El-Haddad, I., Prévôt, A.S.H., 2016. New insights into $PM_{2.5}$ chemical composition and sources in two major cities in China during extreme haze events using aerosol mass spectrometry. Atmos. Chem. Phys. 16, 3207–3225.

Emmons, L.K., Walters, S., Hess, P.G., Lamarque, J.F., Pfister, G.G., Fillmore, D., Granier, C., Guenther, G., Kinnison, D., Laepple, T., Orlando, J., Tie, X., Tyndall, G., Wiedinmyer1, C., Baughcum, S.L., Kloster, S., 2010. Description and evaluation of the Model for Ozone and Related chemical Tracers, version 4 (MOZART-4). Geosci. Model Dev. 3, 43–67.

Fast, J.D., William, I., Gustafson, J., Easter, R.C., Zaveri, R.A., Barnard, J.C., Chapman, E. G., Grell, G.A., Peckham, S.E., 2006. Evolution of ozone, particulates, and aerosol direct radiative forcing in the vicinity of Houston using a fully coupled meteorology-chemistry-aerosol model. J. Geophys. Res. Atmospheres 111.

Gao, M., Beig, G., Song, S.J., Zhang, H.L., Hu, J.L., Ying, Q., Liang, F.C., Liu, Y., Wang, H. K., Lu, X., Zhu, T., Carmichael, G.R., Nielsen, C.P., McElroy, M.B., 2018. The impact of power generation emissions on ambient $PM_{2.5}$ pollution and human health in China and India. Environ. Int. 121, 250–259.

Ge, X.L., Li, L., Chen, Y.F., Chen, H., Wu, D., Wang, J.F., Xie, X.C., Ge, S., Ye, Z.L., Xu, J. Z., Chen, M.D., 2017. Aerosol characteristics and sources in Yangzhou, China resolved by offline aerosol mass spectrometry and other techniques. Environ. Pollut. 225, 74–85.

Gochis, D.J., Coen, J.L., Gill, D.O., Dudhia, J., Davis, C.A., Skamarock, W.C., Klemp, J.B., Powers, J.G., Ahmadov, R., Peckham, S.E., Grell, G.A., Michalakes, J., Trahan, S., Benjamin, S.G., Alexander, C.R., Dimego, G.J., Wang, W., Schwartz, C.S., Romine, G. S., Liu, Z., Snyder, C., Chen, F., Barlage, M.J., Yu, W., Duda, M.G., 2017. The weather research and forecasting model, overview, system efforts, and future directions. Bulletin of the Am. Meteorol. Soc. 98, 1717–1737.

Grell, G.A., Dévényi, D., 2002. A generalized approach to parameterizing convection combining ensemble and data assimilation techniques. Geophys. Res. Lett. 29, 38-1-38-4.

Grell, G.A., Peckham, S.E., Schmitz, R., McKeen, S.A., Frost, G., Skamarock, W.C., Eder, B., 2005. Fully coupled "online" chemistry within the WRF model. Atmos. Environ. 39, 6957–6975.

Guan, W.J., Zheng, X.Y., Chung, K.F., Zhong, N.S., 2016. Impact of air pollution on the burden of chronic respiratory diseases in China, time for urgent action. The Lancet 388, 1939–1951.

Guenther, A., Karl, T., Harley, P., Wiedinmyer, C., Palmer, P.I., Geron, C., 2006. Estimates of global terrestrial isoprene emissions using MEGAN (Model of Emissions of Gases and Aerosols from Nature). Atmos. Chem. Phys 6, 3181–3210.

Han, Z.W., Xie, Z.X., Wang, G.H., Zhang, R.J., Tao, J., 2016. Modeling organic aerosols over east China using a volatility basis-set approach with aging mechanism in a regional air quality model. Atmos. Environ. 124, 186–198.

Hodzic, A., Jimenez, J.L., Madronich, S., Canagaratna, M.R., DeCarlo, P.F., Kleinman, L., Fast, J., 2010. Modeling organic aerosols in a megacity, potential contribution of semi-volatile and intermediate volatility primary organic compounds to secondary organic aerosol formation. Atmos. Chem. Phys. 10, 5491–5514.

Hu, J.L., Huang, L., Chen, M.D., Liao, H., Zhang, H.L., Wang, S.X., Zhang, Q., Ying, Q., 2017. Premature mortality attributable to particulate matter in china, source contributions and responses to reductions. Environ. Sci. Technol. 51, 9950–9959.

Huang, L., An, J.Y., Koo, B.Y., Yarwood, G., Yan, R.S., Wang, Y.J., Huang, C., Li, L., 2019. Sulfate formation during heavy winter haze events and the potential contribution from heterogeneous SO2 + NO2 reactions in the Yangtze River Delta region. China. Atmos. Chem. Phys. 19, 14311–14328.
Huang, L., Zhu, Y.H., Zhai, H.H., Xue, S.H., Zhu, T.Y., Shao, Y., Liu, Z.Y., Emery, C., Yarwood, G., Wang, Y., Fu, J., Zhang, K., Li, L., 2021. Recommendations on benchmarks for numerical air quality model applications in China – Part 1, PM2.5 and chemical species. Atmos. Chem. Phys. 21, 2725–2743.
Iacono, M.J., Delamere, J.S., Mlawer, E.J., Shephard, M.W., Clough, S.A., Collins, W.D., 2008. Radiative forcing by long-lived greenhouse gases, Calculations with the AER radiative transfer models. J. Geophys. Res. 113, D13103.
Jimenez, P.A., Dudhia, J., González-Rouco, J.F., Navarro, J., Montávez, J.P., Garcia-Bustamante, A.E., 2012. A revised scheme for the WRF surface layer formulation. Mon. Weather Rev. 140, 898–918.
Kampf, C.J., Waxman, E.M., Slowik, J.G., Dommen, J., Pfaffenberger, L., Praplan, A.P., Prevot, A.S., Baltensperger, U., Hoffmann, T., Volkamer, R., 2013. Effective Henry's law partitioning and the salting constant of glyoxal in aerosols containing sulfate. Environ. Sci. Technol. 47, 4236–4244.
Knote, C., Hodzic, A., Jimenez, J.L., Volkamer, R., Orlando, J.J., Baidar, S., Brioude, J., Fast, J., Gentner, D.R., Goldstein, A.H., Hayes, P.L., Knighton, W.B., Oetjen, H., Setyan, A., Stark, H., Thalman, R., Tyndall, G., Washenfelder, R., Waxman, E., Zhang, Q., 2014. Simulation of semi-explicit mechanisms of SOA formation from glyoxal in aerosol in a 3-D model. Atmos. Chem. Phys. 14, 6213–6239.
R, Li, M, Peng, W, Zhao, G, Wang, J, Hao, Measurement Report, Rapid changes of chemical characteristics and health risks for high time-resolved trace elements in $PM_{2.5}$ in a typical industrial city response to stringent clean air actions. EGUsphere preprint 2022.
Li, N., Fu, T.M., Cao, J.J., Lee, S.C., Huang, X.F., He, L.Y., Ho, K.F., Fu, J.S., Lam, Y.F., 2013. Sources of secondary organic aerosols in the Pearl River Delta region in fall, contributions from the aqueous reactive uptake of dicarbonyls. Atmos. Environ. 76, 200–207.
Li, N., He, Q.Y., Greenberg, J., Guenther, A., Li, J.Y., Cao, J.J., Wang, J., Liao, H., Wang, Q.Y., Zhang, Q., 2018. Impacts of biogenic and anthropogenic emissions on summertime ozone formation in the Guanzhong Basin. China. Atmos. Chem. Phys. 18, 7489–7507.
Li, G., Zavala, M., Lei, W., Tsimpidi, A.P., Karydis, V.A., Pandis, S.N., Canagaratna, M.R., Molina, L.T., 2011. Simulations of organic aerosol concentrations in Mexico City using the WRF-Chem model during the MCMA-2006/MILAGRO campaign. Atmos. Chem. Phys. 11, 3789–3809.
Li, M., Zhang, Q., Kurokawa, J.I., Woo, J.H., He, K.B., Lu, Z.F., Ohara, T., Song, Y., Streets, D.G., Carmichael, G.R., Cheng, Y.F., Hong, C.P., Huo, H., Jiang, X.J., Kang, S. C., Liu, F., Su, H., Zheng, B., 2017. MIX, a mosaic Asian anthropogenic emission inventory under the international collaboration framework of the MICS-Asia and HTAP. Atmos. Chem. Phys 17, 935–963.
Lin, A.Q., Zeng, Z.T., Xu, Z.Y., Li, X.D., Chen, X.W., Xu, W.J., Liang, J., Chen, G.J., Li, X., Shi, Z., Li, S., Li, J.J., Zeng, G.M., 2021. Changes in the PM2.5-related environmental health burden caused by population migration and policy implications. J. Clean. Prod. 287, 125051.
Ling, Z.H., Xie, Q.Q., Shao, M., Wang, Z., Wang, T., Guo, H., Wang, X.M., 2020. Formation and sink of glyoxal and methylglyoxal in a polluted subtropical environment, observation-based photochemical analysis and impact evaluation. Atmos. Chem. Phys. 20, 11451–11467.
Ma, Y.P., Fu, T.M., Tian, H., Gao, J., Hu, M., Guo, J.P., Zhang, Y.M., Sun, Y.L., Zhang, L. J., Yang, X., Wang, X.F., 2020. Emergency response measures to alleviate a severe haze pollution event in northern china during december 2015, assessment of effectiveness. Aerosol. Air Qual. Res. 20, 2098–2116.
Maji, K.J., 2020. Substantial changes in PM(2.5) pollution and corresponding premature deaths across China during 2015–2019: A model prospective. Sci. Total Environ. 729, 138838.
Maji, K.J., Ye, W.F., Arora, M., Shiva Nagendra, S.M., 2018. PM2.5-related health and economic loss assessment for 338 Chinese cities. Environ. Int. 121, 392–403.
Matsui, H., Koike, M., Kondo, Y., Takami, A., Fast, J.D., Kanaya, Y., Takigawa, M., 2014. Volatility basis-set approach simulation of organic aerosol formation in East Asia, implications for anthropogenic–biogenic interaction and controllable amounts. Atmos. Chem. Phys. 14, 9513–9535.
Morrison, H., Thompson, G., Tatarskii, V., 2009. Impact of Cloud Microphysics on the Development of Trailing Stratiform precipitation in a simulated squall line, comparison of one- and two-moment schemes. Mon. Weather Rev. 137, 991–1007.
Nakanishi, M., Niino, H., 2006. An Improved Mellor-Yamada Level-3 Model, Its Numerical Stability and Application to a Regional Prediction of Advection Fog. Bound.-Lay. Meteorol. 119, 397–407.
Odum, J.R., Hoffmann, T., Bowman, F., Collins, D., Flagan, R.C., Seinfeld, J.H., 1996. Gas/particle partitioning and secondary organic aerosol yields. Environ. Sci. Technol. 30, 2580–2585.
Pathak, R.K., Wu, W.S., Wang, T., 2009. Summertime $PM_{2.5}$ ionic species in four major cities of China, nitrate formation in an ammonia-deficient atmosphere. Atmos. Chem. Phys. 9, 1711–1722.
Pathak, R.K., Wang, T., Wu, W.S., 2011. Nighttime enhancement of $PM_{2.5}$ nitrate in ammonia-poor atmospheric conditions in Beijing and Shanghai, Plausible contributions of heterogeneous hydrolysis of N_2O_5 and HNO_3 partitioning. Atmos. Environ. 45, 1183–1191.
Qi, C., Fu, T.M., Hu, J.L., Qi, Y., Lin, Z., 2017. Modelling secondary organic aerosols in China. Natl. Sci. Rev. 4, 806–809.
Qiu, X.H., Wang, S.X., Ying, Q., Duan, L., Xing, J., Cao, J.Y., Wu, D., Li, X.X., Cheng, Z.X., Yan, X., Liu, C., Hao, J.M., 2020. Importance of wintertime anthropogenic glyoxal and methylglyoxal emissions in beijing and implications for secondary organic aerosol formation in megacities. Environ. Sci. Technol. 54, 11809–11817.
Robinson, A.L., Donahue, N.M., Shrivastava, M.K., Weitkamp, E.A., Sage, A.M., Grieshop, A.P., Lane, T.F., Pandis, S.N., Pierce, J.R., 2007. Rethinking organic aerosols, semivolatile emissions and photochemical aging. Science 315, 1259–1262.
Sander, R., 2015. Compilation of Henry's law constants (version 4.0) for water as solvent. Atmos. Chem. Phys. 15, 4399–4981.
Seinfeld, J.H., Pandis, S.N., 2006. Atmospheric Chemistry and Physics, From air pollution to climate change, Third edition. John Wiley, New York.
Shen, F.Z., Zhang, L., Jiang, L., Tang, M.Q., Gai, X.Y., Chen, M.D., Ge, X.L., 2020. Temporal variations of six ambient criteria air pollutants from 2015 to 2018, their spatial distributions, health risks and relationships with socioeconomic factors during 2018 in China. Environ. Int. 137, 105556.
Shrivastava, M., Fast, J., Easter, R., Gustafson, W.I., Zaveri, R.A., Jimenez, J.L., Saide, P., Hodzic, A., 2011. Modeling organic aerosols in a megacity, comparison of simple and complex representations of the volatility basis set approach. Atmos. Chem. Phys. 11, 6639–6662.
Shrivastava, M., Andreae, M.O., Artaxo, P., Barbosa, H.M.J., Berg, L.K., Brito, J., Ching, J., Easter, R.C., Fan, J., Fast, J.D., Feng, Z., Fuentes, J.D., Glasius, M., Goldstein, A.H., Alves, E.G., Gomes, H., Gu, D., Guenther, A., Jathar, S.H., Kim, S., Liu, Y., Lou, S., Martin, S.T., McNeill, V.F., Medeiros, A., de Sa, S.S., Shilling, J.E., Springston, S.R., Souza, R.A.F., Thornton, J.A., Isaacman-VanWertz, G., Yee, L.D., Ynoue, R., Zaveri, R.A., Zelenyuk, A., Zhao, C., 2019. Urban pollution greatly enhances formation of natural aerosols over the Amazon rainforest. Nat. Commun. 10, 1046.
Tang, L., Qu, J.B., Mi, Z.F., Bo, X., Chang, X.Y., Anadon, L.D., Wang, S.Y., Xue, X.D., Li, S. B., Wang, X., Zhao, X.H., 2019. Substantial emission reductions from Chinese power plants after the introduction of ultra-low emissions standards. Nat. Energy 4, 929–938.
Tsimpidi, A.P., Karydis, V.A., Zavala, M., Lei, W., Molina, L., Ulbrich, I.M., Jimenez, J.L., Pandis, S.N., 2010. Evaluation of the volatility basis-set approach for the simulation of organic aerosol formation in the Mexico City metropolitan area. Atmos. Chem. Phys. 10, 525–546.
Wang, G.H., Zhang, R.Y., Gomez, M.E., Yang, L., Levy Zamora, M., Hu, M., Lin, Y., Peng, J.F., Guo, S., Meng, J.J., Li, J.J., Cheng, C.L., Hu, T.F., Ren, Y.Q., Wang, Y., Gao, J., Cao, J., An, Z.S., Zhou, W.J., Li, G.H., Wang, J.Y., Tian, P.F., Marrero-Ortiz, W., Secrest, J., Du, Z.F., Zheng, J., Shang, D.J., Zeng, L.M., Shao, M., Wang, W. G., Huang, Y., Wang, Y., Zhu, Y.J., Li, Y.X., Hu, J.X., Pan, B., Cai, L., Cheng, Y.T., Ji, Y.M., Zhang, F., Rosenfeld, D., Liss, P.S., Duce, R.A., Kolb, C.E., Molina, M.J., 2016. Persistent sulfate formation from London Fog to Chinese haze. Proc. Natl. Acad. Sci. 113, 13630–13635.
Wiedinmyer, C., Akagi, S.K., Yokelson, R.J., Emmons, L.K., Al-Saadi, J.A., Orlando, J.J., Soja, A.J., 2011. The Fire INventory from NCAR (FINN), a high resolution global model to estimate the emissions from open burning. Geosci. Model Dev. 4, 625–641.
Wild, O., Zhu, X., Prather, M.J., 2000. Fast-J, accurate simulation of in- and below-cloud photolysis in tropospheric chemical models. J. Atmos. Chem. 37, 245–282.
Wu, W.J., Yao, M.H., Yang, X.C., Hopke, P.K., Choi, H., Qiao, X., Zhao, X., Zhang, J.Y., 2021. Mortality burden attributable to long-term ambient PM2.5 exposure in China, using novel exposure-response functions with multiple exposure windows. Atmos. Environ. 246, 118098.
Wu, Y., Zhang, S.J., Hao, J.M., Liu, H., Wu, X.M., Hu, J.N., Walsh, M.P., Wallington, T.J., Zhang, K.M., Stevanovic, S., 2017. On-road vehicle emissions and their control in China, a review and outlook. Sci. Total Environ. 574, 332–349.
Xing, L., Wu, J., Elser, M., Tong, S.R., Liu, S.X., Li, X., Liu, L., Cao, J.J., Zhou, J.M., El-Haddad, I., Huang, R.J., Ge, M.F., Tie, X.X., Prévôt, A.S.H., Li, G.H., 2019. Wintertime secondary organic aerosol formation in Beijing–Tianjin–Hebei (BTH), contributions of HONO sources and heterogeneous reactions. Atmos. Chem. Phys. 19, 2343–2359.
Yin, S.S., Huang, Z.J., Zheng, J.Y., Huang, X.B., Chen, D.H., Tan, H.B., 2018. Characteristics of inorganic aerosol formation over ammonia-poor and ammonia-rich areas in the Pearl River Delta region. China. Atmos. Environ. 177, 120–131.
Zaveri, R.A., Easter, R.C., Fast, J.D., Peters, L.K., 2008. Model for simulating aerosol interactions and chemistry (MOSAIC). J. Geophys. Res. 113, D13204.
Zhai, S.X., Jacob, D.J., Wang, X., Shen, L., Li, K., Zhang, Y.Z., Gui, K., Zhao, T.L., Liao, H., 2019. Fine particulate matter ($PM_{2.5}$) trends in China, 2013–2018, separating contributions from anthropogenic emissions and meteorology. Atmos. Chem. Phys. 19, 11031–11041.
Zhai, S., Jacob, D.J., Wang, X., Liu, Z., Wen, T., Shah, V., Li, K., Moch, J.M., Bates, K.H., Song, S., Shen, L., Zhang, Y., Luo, G., Yu, F., Sun, Y., Wang, L., Qi, M., Tao, J., Gui, K., Xu, H., Zhang, Q., Zhao, T., Wang, Y., Lee, H.C., Choi, H., Liao, H., 2021. Control of particulate nitrate air pollution in China. Nat. Geosci. 14, 389–395.
Zhang, H.R., Li, N., Tang, K.Q., Liao, H., Shi, C., Huang, C., Wang, H.L., Guo, S., Hu, M., Ge, X.L., Chen, M.D., Liu, Z.X., Yu, H., Hu, J.L., 2021a. Estimation of Secondary $PM_{2.5}$ in China and the United States using a Multi-Tracer Approach. Atmos. Chem. Phys. 22, 5495–5514.
Zhang, H.R., Tang, K.Q., Feng, W.H., Yan, X.T., Liao, H., Li, N., 2021b. Impact of Short-Term Emission Control Measures on Air Quality in Nanjing During the Jiangsu Development Summit. Front. Environ. Sci. 9, 693513.
Zhang, Q., Zheng, Y., Tong, D., Shao, M., Wang, S., Zhang, Y., Xu, X., Wang, J., He, H., Liu, W., Ding, Y., Lei, Y., Li, J., Wang, Z., Zhang, X., Wang, Y., Cheng, J., Liu, Y., Shi, Q., Yan, L., Geng, G., Hong, C., Li, M., Liu, F., Zheng, B., Cao, J., Ding, A., Gao, J., Fu, Q., Huo, J., Liu, B., Liu, Z., Yang, F., He, K., Hao, J., 2019. Drivers of

improved $PM_{2.5}$ air quality in China from 2013 to 2017. Proc. Natl. Acad. Sci. 116, 24463–24469.
Zheng, B., Zhang, Q., Zhang, Y., He, K.B., Wang, K., Zheng, G.J., Duan, F.K., Kimoto, T., 2015. Heterogeneous chemistry, a mechanism missing in current models to explain secondary inorganic aerosol formation during the January 2013 haze episode in North China. Atmos. Chem. Phys. 15, 2031–2049.
Zhou, Y.D., Zhao, Y., Mao, P., Zhang, Q., Zhang, J., Qiu, L.P., Yang, Y., 2017. Development of a high-resolution emission inventory and its evaluation and application through air quality modeling for Jiangsu Province. China. Atmos. Chem. Phys. 17, 211–233.